Hard X-ray Emission from the Galactic Ridge

銀河円盤からの硬X線放射

山 崎 典 子

Hard X-ray Emission from the Galactic Ridge

Noriko Y. Yamasaki

December 21, 1995

Abstract

The hard X–ray and γ-ray emission from the Galactic ridge has been studied with the *LAC* instrument on *Ginga* satellite and a balloon born detector *Welcome−1* . From scanning observation along the Galactic plane carried by the *LAC*, a diffuse hard X-ray emission above 10 keV has been significantly detected from extended region along the plane. The spectrum shows a power-law shape with photon index $\alpha = 2.2 \pm 0.2$ and the emission clearly exceeds the single temperature thermal bremsstrahlung. The estimated luminosity of the Galactic ridge between 3keV and 10 keV is 2×10^{38} erg sec^{-1}. We also obtain an upper limit for the Galactic ridge emission between 50keV and 600keV from the γ-ray observation. These results strongly suggests that there is a continuous single power-law emission over keV $\sim$ GeV range from an extended region in the Galactic ridge. Electron bremsstrahlung is shown to be the most likely process. These features can be interpreted if low energy electrons are continuously supplied in the interstellar space. We propose a scenario that shock acceleration of the thermal electrons in hot plasma in SNRs produces fresh supply of cosmic ray electrons.

Contents

List of Figures

List of Tables

<div style="page-break"></div>

Chapter 1

Introduction

The intense emission from the Galactic ridge has been observed in a very wide energy range, from radio up to a few GeV γ-rays. In X-ray band, strong iron line emission along the Galactic ridge found by *Tenma* reveals that diffuse hot plasma with temperature of several keV spreads widely in the Galactic plane. There is definitely a thermal component in the Galactic ridge emission. However, the hot gas is confined in the Galactic plane or it is flow out is a important question to be answered with new observations because such hot gas cannot be bound by the gravitation of the Galaxy.

Diffuse γ–ray and radio emission is considered to be generated by high energy cosmic ray electrons in the interstellar space. These electrons are thought to be accelerated in the interstellar space or in supernova remnants (SNRs). However, the origin of the seed electrons and actual process and the cite of the acceleration are still highly ambiguous.

In the theoretical side, several models have been proposed to account for the diffuse γ-ray emission. These models usually assume a power-law spectrum of high energy electrons and the appropriate spatial distribution of the interstellar matter. However, there has been no quantitative study made on the source of the high energy electrons and their possible relation to the hot plasma.

The purpose of this thesis is to study the origin of the diffuse X-ray and γ-ray emission from the Galactic plane based on the new observational features. The most

1

efficient energy band to investigate the relation between the thermal X-ray and the non-thermal γ-ray emission is the hard X-ray to soft γ-ray band. Observations in these energy bands should bring us information about the possible link. The thermal emission represented by the strong iron K lines becomes very weak above 10 keV. The γ-ray study of the Galactic plane have been carried out only above 35 MeV. Therefore, the hard X-ray band is in a sense an unexplored frontier in the study of diffuse Galactic emission.

The most sensitive instruments in the respective energy bands have been in cooperated in the present observational study. The hard X-ray observation was carried out with the *Ginga LAC* instrument, and the γ-ray observations were done with newly developed balloon detector *Welcome–1* . These instruments provide data with the lowest background so far carried out. The new results thus obtained on the Galactic ridge emission provide rich information with new features in the X-ray to γ-ray spectrum, and enable us to constrain the emission mechanism and make a consistent picture for the emission in the wide energy band.

In Chapter 2, we review past observation of the Galactic ridge in the X-ray and γ-ray bands. Chapter 3 describes X-ray observations from *Ginga*, and Chapter 4 describes that from *Welcome–1* . The observed results are presented in Chapter 5, and the discussions are given in Chapter 6.

Chapter 2

Review of past studies

2.1   Overview

From the beginning of X/γ-ray astronomy, the diffuse emission in the Galactic disk has been attracting interests. In the observation of the Galactic ridge emission, the separation from the background radiation caused by numerous point sources distributed over the Galactic plane is a necessary procedure. This separation requires careful study of the detector itself, for example, the angular response for the point sources and the non X-ray background . Furthermore, the Cosmic X/γ ray background and the detector's internal background should be subtracted. The reliability of the resultant intensity and spatial distribution of the Galactic ridge emission depends much on the observational condition, the detectors field of view or the imaging capability and the spatial coverage.

As shown in this chapter, however, many attempts have been made to measure the diffuse Galactic ridge emission. The existence of the emission from hot plasma ($kT \sim$several keV) in the X-ray band and the emission in the γ-ray band produced by the cosmic ray electrons has been established. We review here the past observational results and the physical interpretation on the Galactic ridge emission.
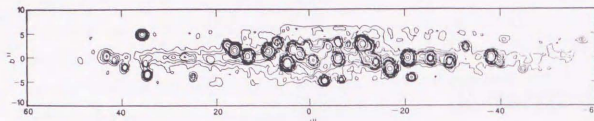
Figure 2.1: Contour map of 2-6 keV X-ray emission in the region
$|l| < 60°$ observed by EXOSAT (Warwick *et al.*, 1985)

2.2   X-ray observations of the Galactic ridge

The diffuse emission from the Galactic ridge in the X-ray band was discovered by
HEAO-1 satellite (Worrall *et al.*, 1982). To subtract the possible point source con-
tamination, they only used the data taken in $l=51° \sim 129°$ and $237° \sim 282°$. Accord-
ing to their results, the scale height of the diffuse emission is 200 ±300 pc, its surface
brightness between 2 and 10 keV, 1×10^{-8} erg cm^{-2} sec^{-1}, and its total luminosity ,
about 1×10^{38} erg sec^{-1}.

EXOSAT scanned the Galactic plane and detected diffuse emission together with
70 resolved point sources (Warwick *et al.*, 1988; Warwick *et al.*, 1985) as shown in
figure 2.1. They measured the spatial distribution of the X-ray ridge emission as a
thin (scale height$\sim$ 100pc) disk with a radius 6.5kpc. This model gives a volume
emissivity of about 6×10^{27} erg s^{-1} pc^{-3} and the total luminosity of 1×10^{38} erg s^{-1}
(Warwick *et al.*, 1985).

Tenma satellite discovered strong 6.7 keV emission lines corresponding to K X-
rays of the He-like ionized iron from the Galactic ridge (Koyama *et al.*, 1986; Koyama,
1989). They observed energy spectra in selected source-free regions along the Galactic
plane finding 6.7 keV line emission with equivalent widths of 400 $\sim$700 eV in most of
region (Koyama *et al.*, 1986). It indicates a thermal emission from optically thin hot
plasma with $kT = 5 \sim 10$ keV. At some location, silicon and sulfur lines are detected
near the statistical limit suggesting that the hot plasma could be in ionization non-

equilibrium state The spatial distribution of the emission is consistent with a disk-
shape emission having a scale height of 100-300 pc and a radius of 10 kpc. The average
luminosity per unit surface is $(2.4\sim2.8)\times10^{29}$ erg s^{-1} pc^{-2} and the total luminosity
between 2 keV and 10 keV is about 10^{38} erg s^{-1}. *Tenma* observations have made a
significant progress to the understanding of the ridge emission.

The 6.7 keV line intensity was mapped in the Galactic center region and along
the Galactic plane by the *Ginga* satellite (Koyama *et al.*, 1989; Yamauchi *et al.*,
1990; Yamauchi, 1991). This observation shows that there are a strong iron-line
emitting region at the galactic center with an elliptical shape of $1.8°\times1.0°$, and a
bulge emission with an elliptical shape of $10°\times5°$. The energy spectra from point-
source-free regions in the Galactic ridge region ($20° < l <40°$) between 1 keV and
10 keV also show strong 6.7 keV line emission with equivalent width of 560 $\sim$ 1800
eV. The fitting the continuum spectra with thermal bremsstrahlung model gives the
temperature of $4 \sim 9$ keV. They concluded that the spatial distribution of the 6.7
keV line emission is well represented by a thin disk component with a scale height
of 100 pc and a radius of 4kpc and with addition of a galactic arm component at
$l = \pm30°$ (Yamauchi, 1991; Yamauchi and Koyama, 1993).

The observed flux of the Galactic ridge emission are summarized in table 2.1. The
flux is shows as a surface brightness at the Galactic center.

2.2.1   Interpretation of the X-ray emission from the Galac-
tic ridge

The observed X-ray emission from the Galactic ridge has been interpreted in terms
of two different ways. One is that the ridge emission consists of unresolved numerous
faint point sources. The other is that it is of truly diffuse origin.

When *HEAO-1* first detected the emission from the Galactic plane, the emission
being of discrete origin seemed more promising than of diffuse origin (Worrall *et al.*,
1982) because the detection sensitivity was thought to have been left many hidden
point sources undetected below the detection limit. The luminosity required for the
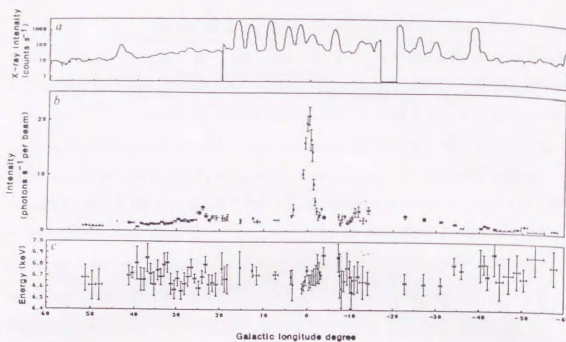
Figure 2.2: Fe fluorescent line map obtained by *Ginga* (Koyama *et al.*, 1989)(a) scan profile of the X-ray emission in 2-18keV (b) that of the iron line emission (c) the line energy

contributed point sources was $L_X < 9.0 \times 10^{34}$erg s^{-1} and the number density was $\rho > 1.4 \times 10^{-6}$ pc^{-2} (Worrall *et al.*, 1982).

Tenma's discovery of the strong 6.7 keV line emission from hot plasma gave constraints to the energy spectrum of these unresolved point sources. If both the continuum emission and the iron K-line emission come from the same point sources, the energy spectrum of the possible point sources has a shape of thin thermal bremsstrahlung with temperature $kT = 5 \sim 10$ keV and contains strong (EW$\sim$500eV) 6.7 keV iron emission line. The major candidates were RS CVn stars and cataclysmic variables (CVs) because of the similarity of this spectral feature (Koyama *et al.*, 1989; Yamauchi, 1991). As the luminosity of these sources are smaller than 1×10^{33}erg sec^{-1}, the number density or the spatial distribution were under study. The contribution of these sources to the Galactic ridge emission was still uncertain.

If the Galactic ridge emission is of diffuse origin, according to Worrall *et al.*

Mission/detector (reference)	Energy range (keV)	field of view	observation field	surface brightness (erg cm^{-2}sec^{-1}) ph cm^{-2}sec^{-1}MeV^{-1}str^{-1}	point source subtraction
Exosat (Warwick *et al.*, 1985)	$2\sim6$	$0.75° \times 0.75°$	$|l| <40°$ $|b| <5$ °	$(3\times10^{-11}$beam$^{-1})$ $\rightarrow 7\times10^3$	done (scan)
Tenma (Koyama *et al.*, 1986)	$1.6\sim14$	$3.1°$	8 blank point in $280° < l <340°$ $-5° < b <5°$	$(8\times10^{-8}$str$^{-1})$ $\rightarrow 5\times10^2$	no
HEAO-1 A2 (Worrall *et al.*, 1982)	$2\sim10$	$1.5° \times 3°$	$51° < l <282°$ $-12° < b <12°$ known source≤ 2	$(6\pm1.6)\times10^1$ ($@l =60°$,E=10keV)	no
Ginga (Yamauchi 1991)	$1.2\sim10$ (keV)	$1.08° \times 2.0°$	$-15° < l <20°$ $-10° < b <15°$	3×10^{-28}erg s^{-1}cm^{-3} (volume emissivity)	no

Table 2.1: Summary of the observed flux of the X-ray Galactic ridge emission

(1982) Cosmic electrons become its source through two emission mechanisms; the synchrotron emission in the magnetic field and inverse Compton scattering with soft (such as starlight, infrared) photons. The expected X-ray continuum flux by the observed cosmic electron flux falls, however, short of the observed one in either emission mechanisms (Worrall *et al.*, 1982). If the continuum emission from the Galactic ridge also comes from the thin hot plasma as implied by the iron K-line emission, the temperature of the plasma is $kT = 5\sim10$ keV and the electron density calculated by the surface brightness is $n_e = 10^{-3}$ cm^{-3}. This gives a pressure of $(p/k) = 10^5$ cm^{-3}K and a thermal velocity of 10^8 cm sec^{-1}. When *HEAO-1* discovered the Galactic ridge emission, the existence of such a hot gas in the interstellar medium seemed to be unlikely because the pressure is much higher than the general value of ≤ 2000 cm^{-3}K in the interstellar space (Worrall *et al.*, 1982) and the thermal velocity exceeds the escape velocity from the Galactic plane of 10^6 cm sec^{-1}. However, the discovery of the 6.7 keV line by *Tenma* has clearly shown the existence of the hot plasma.

To explain the origin of the hot plasma filling the Galactic plane, shock heated hot gas in supernova remnants (SNRs) has been proposed (Koyama *et al.* 1986; Koyama, Ikeuchi and Tomisaka 1986). Koyama, Ikeuchi and Tomisaka (1986) have shown that the condition of SNRs whose radio flux falls under the detection limit but X-ray flux is enough to contribute to the ridge emission is that the age is $t = 10^4$ year and the gas density at the shock front is $n_s = 0.4$ cm^{-3}.

One feature implied from this model is that the plasma is still in an ionization non-equilibrium phase. In the energy spectrum of the ridge emission, *Tenma* detected sulphur and silicon emission line (Koyama *et al.*, 1986). The iron line energy and equivalent width obtained by *Ginga* from the source-free region in the Galactic plane suggest that the ion temperature is significantly lower than the electron temperature (Yamauchi and Koyama, 1995). It is suggested that the emission region does not reach ionization equilibrium state in agreement with the interpretations by Koyama *et al.* (1986). The idea of shock heated plasma as origin of the ridge emission is attractive to explain the spectral feature .

On the other hand there remain two problems. Firstly the typical temperature of X-ray detected SNRs is below 1 keV. The number of the detected SNRs whose temperature is higher than 1keV is relatively small and the process how shock front can heat the gas up to several keV in SNRs is not clear. Secondly the supernova rate required by the total luminosity of the ridge emission is one per 10 year, much higher than the current estimation of one per 30 year.

In summary, if the ridge emission is of discrete origin, most probable candidates are RS CVns and CVs. The estimation of the contribution of these sources to the ridge emission is uncertainties. If the ridge emission is of diffuse origin, the existence of thin hot plasma with temperature of 5~10 keV is required. Shock heated plasma in SNRs would satisfy to explain the spectral feature however, the heating process and the total energy supply is still under study.

2.3 Gamma-ray emission from the Galactic ridge

2.3.1 Discovery of the diffuse γ ray emission

Emission along the Galactic plane has also been observed in the γ-ray band (Bloemen, 1989). In these γ ray observations, the typical angular resolution is determined by electromagnetic shower tracking devices, the spark chamber to be a few degree. So the observation of the γ ray emission always suffers from background subtraction and the point source contamination.

The intense γ-ray emission from the Galactic plane is observed in early days of the γ-ray astrophysics. The emission has been considered indicative of interaction of cosmic rays with interstellar matter. The first mapping of the γ-ray sky was carried out by *SAS2* between 35 MeV and 200 MeV (Hartman *et al.*, 1979). After subtracting strong point sources such as Vela pulsar and Cygnus X-3, a large part of the emission along the Galactic plane was considered as diffuse origin since the number of point sources detected in the γ-ray band and the source confusion was thought to be small. The average energy spectrum at $335° < l < 15°$ is almost power law shape with a photon index ~ 1.7 without any line features. The flux at 100 MeV is 1×10^{-6} photons cm^{-2} sec^{-1}str^{-1} MeV^{-1}.

COS-B surveyed the Galactic plane in energy ranges between 70 MeV and 5 GeV with higher sensitivity and better angular resolution than *SAS2*. The large scale structure of the Galactic ridge emission in high energy γ ray band was studied precisely as shown in figure 2.3 and the scale height is measured as about 130 pc(Mayer-Hasselwander *et al.*, 1982).

2.3.2 Origin of the γ-ray emission

Three processes have been proposed for the origin of the diffuse γ-ray emission. The first is interaction of cosmic-ray nuclei with interstellar matter, the second is inverse Compton scattering of photons with cosmic-ray electrons, and the third process is bremsstrahlung of cosmic electrons with interstellar matter.
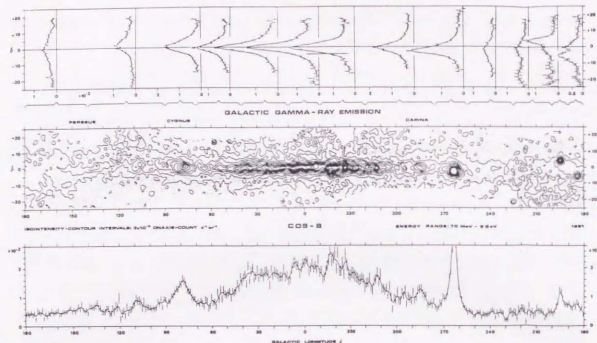
Figure 2.3: *Cos-B* sky map (Mayer-Hasselwander *et al.*, 1982), longitude and latitude profile and a contour map

In the first process, the interaction of cosmic-ray nuclei with interstellar matter, the dominant contribution is considered to come from neutral pions, π^0, created in the collision. The pions decay into two gamma ray photons, $\pi^0 \rightarrow 2\gamma$, in a short life time of 1.8×10^{-18} seconds. The energy of γ-ray is 68 MeV in the rest frame of the π^0 which transforms into a broad energy distribution centered on ~ 68 MeV. The spectra observed by *COS-B* (Paul *et al.*, 1978) as well as a balloon-borne spark chamber experiment (Bertsch and Kniffen, 1983) show no spectral features characteristic of the π^0 decay; a shoulder around 70 MeV. These results limit the contribution of π^0 decay emission.

In the second process, soft photons scattered by the cosmic electrons are considered to come from the cosmic microwave background (2.7 K), infrared emission in the interstellar space, and starlight. The density of the cosmic microwave background is well known. The distribution of the starlight and infrared away from the solar system are not yet known accurately.
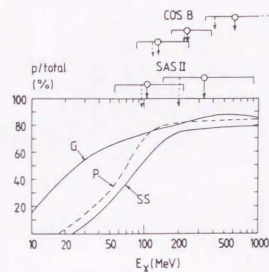
Figure 2.4: The fraction of the γ-ray flux due to protons as a function of γ ray energy (Bhat *et al.* 1984) . G, P, SS:different authors' prediction (G:Goned 1981,P:Poon 1983,SS:Sacher and Schonfelder 1984)

The intensity of the emission from the third process involves the interaction rate between the interstellar matter and the cosmic electrons. The interstellar matter consists mostly of hydrogen occupying about 64 % of the mass (Murthy and Wolfendale, 1993). The distribution of atomic hydrogen (HI) is directly obtained from survey of 21 cm radio wave, but that of molecular hydrogen (H_2) is estimated indirectly from CO line observations in 100 GHz band. We note that there remains some ambiguity on relating CO distribution to that of molecular hydrogen (Murthy and Wolfendale, 1993). However, the correlation between the γ-ray intensity and the HI column density is clearly shown in the *COS-B* observation (see figure 2.5).

We note that the γ-ray emissivity of a nucleus is smaller than an electron of the same energy because of its heavy mass. The estimated fraction of the γ-ray flux due to protons as a function of γ-ray energy is shown in figure 2.4. From these consideration, contributions from protons and nuclei is not dominant in the γ-ray energy below 100 MeV.

From these results and the estimation for the electron emissivity in the interstellar
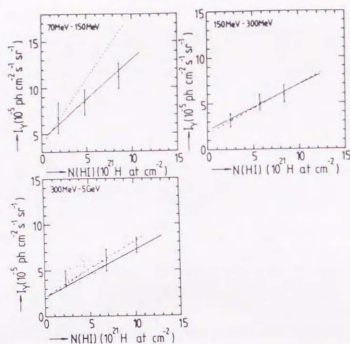
Figure 2.5: Comparison with *COS-B* γ-ray intensities and HI column
densities in the second and third quadrants.(Murthy and
Wolfendale, 1993)

space, the idea of the γ-ray emission below 100 MeV from cosmic electrons is generally
accepted. For detailed studies of the γ-ray emission from the Galactic plane, we should
know the energy spectrum and the spatial distribution of the cosmic electrons.

2.3.3   Energy spectrum cosmic electrons

The observational energy spectrum of cosmic electrons above 5 GeV is summarized
by Nishimura *et al* (1990) as in figure 2.6. The electron spectrum between 30 GeV
and 1 TeV is well represented by (Nishimura *et al.*, 1990)

$$J_e = 1.5\times10^{-4}(E/100GeV)^{-(3.3\pm0.2)}\ \ \mathrm{m}^{-2}\mathrm{sr}^{-1}\mathrm{s}^{-1}\mathrm{GeV}^{-1}\ \ \ (30\mathrm{GeV} < E < 1\mathrm{TeV}).(2.1)$$

The spectrum is a single power-law shape of index 3.3 ± 0.2.

However, the observed electron spectrum below 10 GeV is different with that in the
interstellar space because it is modulated by the magnetic field of the solar system.
There is another way to obtain information on cosmic electrons by observation of
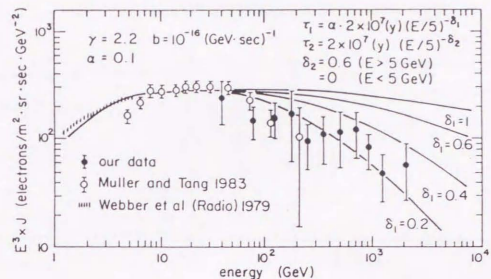
Figure 2.6: The observed spectrum of cosmic electrons (Nishimura *et al.*, 1990)

synchrotron radiation in the radio band in spite of the direct measurement. The
maximum emission frequency ν_m in the equation A.3 for a 5 GeV electron in the
interstellar space with the magnetic field of 3μ Gauss (Allen, 1976) is about 370
MHz. Electrons of a power-law spectrum with index p in the magnetic field radiate
emission of a power-law shape with energy index $(p-1)/2$ as described in Appendix
A. The observed radio spectrum below $\nu <$400 MHz follows a power-law shape with
energy index of 0.8∼0.9 as shown in the left panel of figure 2.7 (Longair, 1994a).
The calculated electron spectrum is shown in the right panel of figure 2.7 taking
into the consideration of the strength of the magnetic field and the emissivity in the
interstellar medium (Longair, 1994a). The overall spectrum between 100 MeV and
100 GeV is gently curved and the index being about 2 between 100 MeV and 1 GeV.

Based on these observational results about the electron spectrum above 100 MeV,
the γ-ray emission from the Galactic ridge above *Cos-B* band is considered to come
from bremsstrahlung of the cosmic electrons as shown in the previous section. A
sample of the estimated γ-ray spectra is shown in figure 2.8. These studies have
shown that the γ-ray spectrum below 100 MeV is dominated by the bremsstrahlung
and inverse Compton scattered photons.
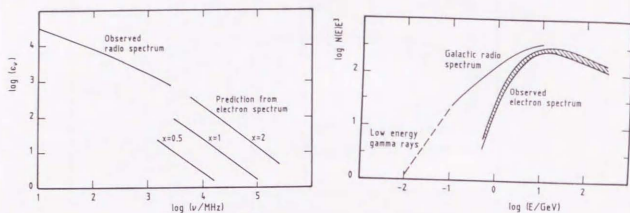
Figure 2.7: Comparison with cosmic rays and expected radio emis-
sion:right panel is the predicted radio spectrum from
the cosmic ray electron (×1 means a uniform magnetic
field of 3μ Gauss,left panel is predicted electron spec-
trum from radio emission and γ-ray emission,the differ-
ence provides a measure of the solar modulation effects
(Longair, 1994a)

The difference of spectral index between below and above 10 GeV is generally
considered to be due to the synchrotron energy loss process (Longair, 1994a; Berezin-
skiĭ *et al.*, 1990). Assuming that the electrons of a single-power law shape with
index p is injected in the interstellar space as a simplest case, they diffuse in the
Galaxy and lose their energy by the synchrotron radiation, inverse Compton scatter-
ing, bremsstrahlung and ionization of the interstellar medium (see Appendix B). If
the diffusion is a dominant process, the shape of the electron spectrum is unchanged
($E_1 < E < E_2$ in figure B.2). As the energy loss rates of the synchrotron radiation
and inverse Compton process are proportional to the electron energy, these process
become dominant in the high energy band and the spectrum is steepened to $p + 1$.
The observed feature of the cosmic electrons is well represented by the interpretation
with detailed consideration. The diffusion time scale is considered to be $10^{14} \sim 10^{15}$
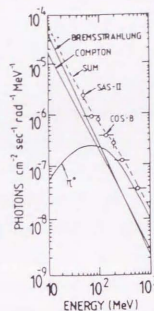
Figure 2.8: A comparison of the observed γ-ray spectrum to the cal-
culated one for $-10° < b < 10°, 320° < l < 40°$. (Kniffen
and Fichtel, 1981)

seconds. Using this time scale and the hydrogen density in the interstellar space,
the energy loss rate of below 100 MeV is dominated by the ionization loss process.
According to these consideration, the electron spectrum below 100 MeV is expected
to be flattened. The estimated mean path length below 4 GeV is about 10 g cm^2
(Webber, 1990). However, the electrons with energy below 100 MeV are not able to
be observed by the synchrotron radiation because the the intensity of thermal radio
emission is stronger than that of synchrotron radio emission below 200 MHz (Longair,
1994a). The γ-ray observation below 100 MeV is considered to be the only way to
get information on the low energy cosmic electrons.

2.3.4 Origin of cosmic ray electrons

The origin of the cosmic rays including electrons is a long standing issue in astro-
physics. As the energy spectrum of the cosmic rays follows power-law shape up to
GeV, an efficient acceleration mechanism has to be working. For cosmic nuclei, both

galactic origin and extra galactic origin are proposed because of their flat distribution in the Galaxy. For cosmic electrons, however, the spatial distribution supports galactic origin. As the energy density of the cosmic rays is as large as 0.5 eV cm^{-3} diffusive shock acceleration in a supernova blast wave is most widely considered. In supernovae remnants repeated crossings of the shock front occurs during a random particle walk, and particles receive an energy gain in the head-on collisions with scattering centers embedded in the background plasma (Ptsukin, 1994). This estimate implies that the release of the energy in the form of the cosmic rays is approximately 3×10^{49} erg or 3 % of the kinetic energy of ejecta. As this process is a version of the first-order Fermi acceleration, energy spectrum of particles becomes a power-law shape. After the acceleration, the particles diffuse into the Galaxy and change their spectrum by escaping from the Galaxy or by losing their energy. For the energy loss process, three processes are proposed such as ionization of the interstellar matter, synchrotron emission, and inverse Compton process.

One of the observational results supporting the acceleration in SNRs is the γ ray emission associated with SNRs. A large feature called North Polar Spur in figure 2.3 and 2.9 (called Loop 1 in the radio band) is identified with an SNR which is centered on a point 130 pc away from the Sun and has a radius of 115 pc at present (Murthy and Wolfendale, 1993). This suggests a high density of electrons in SNRs. However, there has been few direct evidence for such acceleration. There are still many questions concerning the cosmic ray origin such as where the acceleration occurs, what becomes the injection particles, how efficiently the particles obtain energy.

An observational evidence of the acceleration in SNRs

Recent X-ray observations by *ASCA* discovered a non-thermal X-ray emission from a SNR SN1006 (Koyama *et al.*, 1995). It is a typical shell-like SNR observed in X-ray and radio band. The energy spectrum from the rim of SN1006 is well represented by a single power-law of a photon index 2.95±0.20 with two emission lines (K shell resonance transitions of He-like and H-like O). On the other hand, the spectrum from the inner region shows a typical thermal emission of young SNRs. At the same
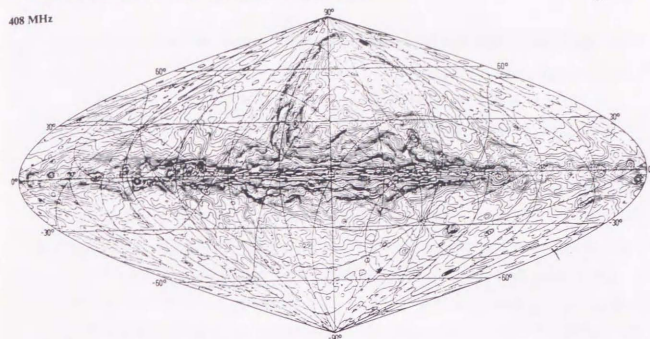
408 MHz

Figure 2.9: Radio intensity map at 408MHz (Verschuur and Kellermann, 1988)

place, strong polarized radio emission is observed indicating strong magnetic field. It strongly supports that the electrons are accelerated to the relativistic energies at the shock front. This is the first direct evidence of the shock acceleration in SNRs. In the X-ray spectrum of other SNRs like Cas A, IC433 and Tycho, there exist data suggesting the non-thermal component. Future spatially resolved X-ray spectroscopy would reveal such non-thermal component indicating the shock acceleration.

2.4   Hard X-ray/low energy γ-ray emission from the Galactic ridge

2.4.1   Hard X-ray/ low energy γ-ray Observation

After the observation by *COS-B* many attempts have been made to measure the Galactic ridge emission in the lower energy regions, because of the interest both in the γ ray emission itself and in the density and spectrum of cosmic ray electrons and its interaction. The γ-ray spectrum gives information on the spectrum of cosmic ray electrons, which may include the information about the acceleration process and the interstellar matter stopping the cosmic electrons. As it is difficult to image or to

map the Galactic plane with low energy γ rays, the observational results are not very consistent with each other.

Mandrou *et al.* (1980) observed diffuse emission by a balloon-borne scintillation detector between 80keV and 8MeV in $-45° < l < 45°$ without considering the point source contribution. A Balloon-borne Ge detector *GRIS* observed the Galactic ridge in $30 \sim 5000$ keV (Gehrels and Tueller, 1993) at $l = 335°$, where a black hole candidate GX339-4 is in the field of view, and obtained harder (photon index ~ 1.5) spectrum than the previous observations. Recently, *Comptel* observed a first MeV image of the Galactic plane (Strong *et al.*, 1994) between 1 MeV and 30 MeV. The spectrum is about a factor 2 lower than that of *GRIS* and lies on a power law (index~ 2) extension of the *COS-B* results. It indicates that the mean path length for the electron below 100 MeV is 8 g cm^{-2}, which is smaller than the expected value (Strong *et al.*, 1994). The detection of the Galactic ridge emission by *OSSE* between 50keV and 1MeV was reported by Purcell (1995). They extracted the point source contribution using the simultaneous observation by *SIGMA*. The resultant spectrum is a single power law shape with a photon index 2.30 ± 0.07 and the intensity is also about half the *GRIS* value (Purcell *et al.*, 1995).

The observed fluxes of the Galactic ridge in γ-ray band are summarized in table 2.2 and in figure 2.10. Note that the flux is normalized to that in the central 1 radian of the Galactic plane, such that

$$F_{rad} = \int_{-1/2}^{1/2} dl \int_{-\pi/2}^{\pi/2} \cos b \, db \, I(l,b) \qquad (2.2)$$

where $I(l,b)$ means the surface brightness at Galactic coordinate (l,b) in a radian.

2.4.2 Interpretation of the hard X-ray/γ ray emission

As shown in the previous section, the observation of the Galactic ridge emission between 10keV and 1MeV still has some uncertainties due to the point source contribution and the wide field of view of the detectors. However, this energy band is the only window to study the properties of the medium-energy cosmic electrons in the Galaxy.

Mission/detector (reference)	Energy range (MeV)	field of view	observation field	flux from the central radian ph cm^{-2}sec^{-1}MeV^{-1}rad^{-1}	point source separation
Gris (Gehrels and Tueller, 1993)	$0.03 \sim 6$	$16°$	$l = 335°$ $b = 0°$	0.31 (@E=100keV)	no
(Mandrou *et al.*, 1980)	$80 \sim 100$ $0.1 \sim 0.15$ $0.15 \sim 0.4$ $0.4 \sim 1.0$	$90°$	$\|l\| < 45°$	0.9 ± 0.2 0.3 ± 0.1 $(2.3\pm0.7)\times10^{-2}$ $(1.0\pm0.4)\times10^{-2}$	no
OSSE (Purcell *et al.*, 1995)	$0.05 \sim 2$	$4° \times 11°$	$20° < l < 30°$ $-2 < b < 2$	0.18 (@E=100keV)	done (SIGMA)
Comptel (Strong *et al.*, 1994)	$0.75 \sim 1$ $1 \sim 3$ $3 \sim 10$ $10 \sim 30$	$\sim 35°$	$\|l\| < 60°$ $\|b\| < 20°$	$(3.9\pm0.8)\times10^{-3}$ $(7.8\pm1.8)\times10^{-4}$ $(6.4\pm1.4)\times10^{-5}$ $(8.1\pm1.8)\times10^{-6}$	done (imaging)
(Bertsch and Kniffen, 1983)	$10 \sim 30$ $30 \sim 50$ $50 \sim 90$	$20°$ (@10MeV) $2°$ (@1GeV)	$20° < l < 45°$ $\|b\| < 5°$	$(2.8\pm1.2)\times10^{-5}$ $(1.0\pm0.6)\times10^{-5}$ $(1.5\pm0.7)\times10^{-6}$	no
SAS-2 (Hartman *et al.*, 1979)	$35 \sim 200$	$2°$	$\|l\| < 60°$ $\|b\| < 10°$	$(2.0\pm0.5)\times10^{-6}$ (@50MeV) $(8.0\pm1.5)\times10^{-7}$ (@100MeV) $(2.6\pm0.6)\times10^{-7}$ (@200MeV)	done
Cos-B (Paul *et al.*, 1978)	$50 \sim 100$ $100 \sim 200$ $200 \sim 400$ $400 \sim 820$ $820 \sim 1640$ $1640 \sim 3300$		$\|l\| < 15°$ $\|b\| < 5°$	$(8.6\pm1.4)\times10^{-7}$ $(3.9\pm0.6)\times10^{-7}$ $(1.3\pm0.2)\times10^{-7}$ $(3.4\pm0.8)\times10^{-8}$ $(7.4\pm3.9)\times10^{-9}$ $(1.3\pm0.7)\times10^{-9}$	done (imaging

Table 2.2: Summary of the observed flux of the γ-ray Galactic ridge emission
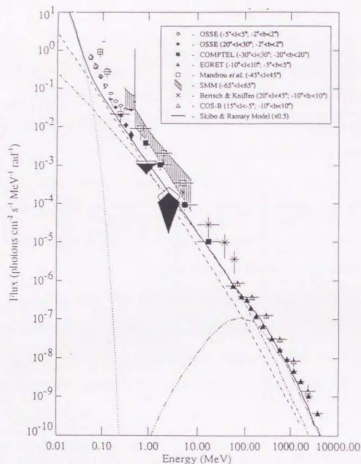
Figure 2.10: The wide band spectrum of the Galactic ridge emission
by Purcell(1995)

Sacher and Schönfelder (1984) calculated the expected low energy γ ray diffuse emission assuming the spectrum of the cosmic ray electrons. As there are a few observational results, they compared the calculated emission with observational results and found that the electron flux would be high enough to be able to explain the ionization rate in HI regions.

Skibo and Ramaty (1993) also calculated the emission spectrum from cosmic ray electrons, assuming that the injection spectrum is an unbroken power-law form between 10 keV and 10^3 GeV and that the electrons propagate in the Galaxy following the leaky box model to yield an equilibrium electron flux. The escape path length for electrons with energy below 3 GeV is taken as a constant 6 g cm^{-2} of interstellar matter. Compared with the observed γ-ray spectrum, the calculated curve provides an acceptable fit to the data except below 0.2 MeV (see curves in figure 2.10). The

diffuse γ-ray emission below 0.2 MeV would be produced by low energy electrons. This model requires a total power input of 4×10^{41} erg sec^{-1} to maintain the population of low energy electrons, which exceeds the total power supply of the nuclear cosmic rays by about an order of magnitude. Unless some special acceleration process is working for electrons, it seems difficult to explain the γ-ray spectrum below 0.2 MeV.

From these studies, low energy γ ray (>1 MeV) emission from the Galactic ridge is mainly produced by the low energy cosmic electrons through bremsstrahlung. However, the distribution and the spectrum of the hard X-ray / low energy γ ray emission (<1 MeV) is still not properly measured. It is very important to know how the apparent thermal spectrum in the soft X-ray band is connected up with the non-thermal spectrum in the γ-ray region. It is expected that a change from the thermal emission to non-thermal emission can be observable in the hard X/γ-ray region. Based on these consideration, we carry out observational study of the hard X-ray emission from the Galactic ridge with *Ginga* ($1 \sim 20$keV) and *Welcome-1* ($50\sim600$keV) in this thesis.

Chapter 3

Observation by Ginga

3.1 Instrumentation

Ginga is the third Japanese X-ray astronomy satellite (Turner *et al.*, 1989) launched on February 5, 1987, from the Kagoshima Space Center by the Institute of Space and Astronautical Science. The apogee and perigee of the initial orbit are 670 and 510 km, respectively, with an inclination of 31 degrees. The orbital period is about 96 minutes. The satellite weighs 420 kg. It reentered to the atmosphere on November 1, 1991.

The Large Area Proportional Counter (hereafter refereed to as *LAC*) experiment is the major scientific instrument on board *Ginga* along with the All Sky Monitor and the Gamma-ray Burst Detector experiments. The *LAC* has been developed under international collaboration between Japan and UK.

The *LAC* consists of 8 proportional counters with total geometrical area of 4000 cm^2. A schematic view of the detector is shown in figure 3.1. The counters are filled with gas consisting of 75 % argon, 20 % xenon and 5 % carbon-dioxide. Each counter has its own high-voltage supply operated normally at $\sim$1830V, and the gain is corrected to 1.0% accuracy using 22.1keV line produced by silver coated on small part of the *LAC* collimators.

The gas volume of the proportional counter is divided by ground wires into 52 cells, each having an anode wire. The cells are grouped into the guard anti counters

(V1 and V2) and the signal layers (L1 R1 S1 and S3) as shown in figure3.1. The signal layers are further divided into the TOP layer (L1 and R1) and the MID layer (S2 and S3). The *LAC* is sensitive in the energy range between 1.2 keV and 37.4 keV. The energy is covered by 48 ADC channels and the energy resolution is 18.0 % at 6keV. The field of view is $1.08° \times 2.0°$(FWHM) with a trapezoid aperture collimated by 25μm stainless steel honeycomb tubes. Using the guard cells as anti coincidence counters, the background level in orbit is about 3.5×10^{-4} counts s^{-1} keV^{-1}. We will later explain the background reduction method in detail. The sensitivity of the *LAC* is shown in figure 3.2.

The definition of satellite coordinates is shown in figure 3.3. A momentum wheel stabilizes the attitude of the spacecraft and control the rotation around Z-axis(slew). The maximum speed of the slew is 14° minutes^{-1}. Three magnetic torquers are used to control the Z-axis direction (maneuver). Using the slew around Z-axis , the spacecraft can be operated in a scanning mode to rotate the Y-face on which the *LAC* is mounted. The accuracy of the attitude control of the spacecraft is about 0.1° and the attitude can be determined in the ground analysis with 0.02 ° accuracy based on the data from four gyroscopes and two star sensors.

3.2 Observation

Observation of the Galactic ridge emission with a non-imaging detector or a detector with a large FOV can be carried out in two ways in general. One is to observe only those ridge regions where no known X-ray sources exist, and the other is to scan the ridge region including point sources and somehow subtract the point source contributions. In the former method, one can select the regions to be observed based on previous X-ray surveys by Einstein for example. This method suffers from possible contamination of faint point sources missed in the previous surveys. These sources often have strongly absorbed energy spectra, which show up in the hard X-ray band where the *LAC* 's sensitivity surpasses all other measurements. In effect, we need to subtract contributions of point sources. Therefore we employ the latter way for the
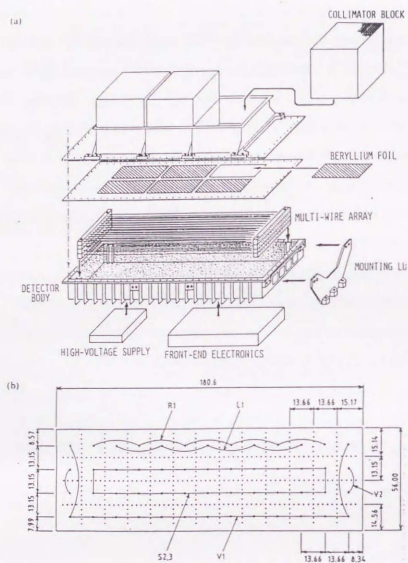
Figure 3.1: Schematic view of one proportional counter of *LAC*
(Turner *et al.*, 1989) upper panel:An exploded view of
a *LAC* detector,lower panel:Cross section of the propor-
tional counter gas cell showing the anode connections

study of the hard X-ray emission in this thesis. The scan data need to be divided
into the flux between the diffuse component and the point source contribution. The
statistics of the data obtained using the *LAC* are high enough to enable such an
analysis with good accuracy.

The *LAC* scanned the Galactic Ridge region 12 times parallel to the Galactic
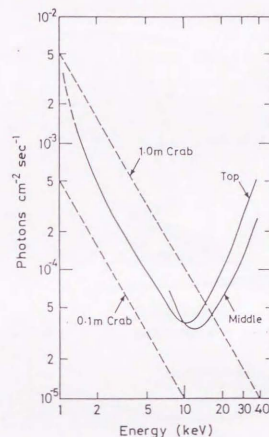
Figure 3.2: 3 σ sensitivity of the *LAC* as a function of energy for top
and middle layers taken from Turner *et al.*1989

plane between 1987 August and 1991 May for total exposure time 2.4Msec. In this
thesis we analyze data taken in the 6 scans, 4 scans passing near the Galactic Center,
1 in the plane away from the Galactic center ($7 < |l| < 40$), and 1 at high latitude
($|b| \sim 10$). The 6 scan paths are shown in figure 3.4 and the observation logs are
summarized in table 3.2.

3.3   Analysis of the scanning data

3.3.1   Outline of the analysis

The analysis of the scan data is performed in the following sequence.

  1. Selection of low background data through several criteria.
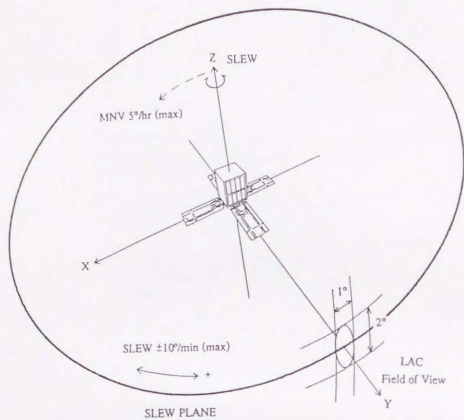
Figure 3.3: The *Ginga* satellite axis and the collimator field of view.
LAC is mounted in the Y-face of the spacecraft.(Turner
et al., 1989)

No.	date	b	l	Bit rate	Obs.time	No.of scans	Scan speed
1	1989 4 5	1.6~2.5	-7.5~7.5	Medium	6.3ksec	17	0.95deg/min
2	1989 4 1	-0.7~-0.7	-8.1~4.1	Low	10.9ksec	19	0.64deg/min
3	1989 4 6	-1.8~2.5	-7.5~2.9	Low	17.8ksec	16	1.38deg/min
4	1989 4 9	-9.8~-9.4	-4.1~3.9	Medium	4.0ksec	12	0.64deg/min
5	1988 3 17	0.4	-14.7~7.5	Medium	10.9ksec	9	1.38deg/min
6	1987 10 9	-0.7~-0.4	20.5~39.	Medium	11.6ksec	12	0.95deg/min

Table 3.1: The Observation log of the Galactic ridge scan used in this analysis
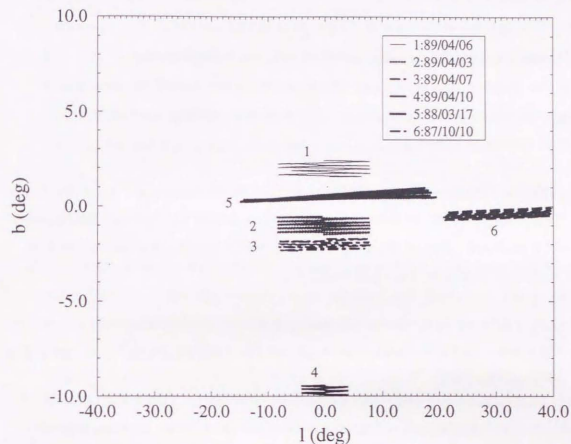
Figure 3.4: Scan paths of the Galactic ridge observations which are analyzed

2. Subtraction of non X-ray background using a model background which is esti-
mated by a function of monitor counts.

3. Subtraction of the CXB.

4. Fitting of the scan data as a sum of point sources and diffuse emission.

In this section, the actual procedure carried out here is described in detail.

3.3.2 Data selection criteria

The non X-ray background in the *LAC* consists of three components according to its origin; (i)those due to cosmic rays, (ii)trapped charged particles and (iii)radio activation. Background in the form of X-rays includes (iv) the cosmic X-ray background (CXB) and (v) the solar X-rays reflected by the sun-lit Earth surface.

In the study of the diffuse X-ray emission, we should selects the data with low background and subtract it effectively. In the present analysis , we apply the data selection criteria as follows ;

1. Limiting the observation mode to the MPC-1 mode only;

   In the MPC-1 mode, events are accumulated separately for TOP and MID layers of 8 counters. This is the mode in which non X-ray background can be best estimated as will be described later.

2. Use only those data when cutoff rigidity is greater than 10GeV/c ;

   This is to minimize background originated by trapped charged particles (ii) (Hayashida, 1989).

3. Use only those data when the elevation angle of the detector direction is greater than 10° above the earth rim;

   This is to minimize the background contamination by solar-X ray reflected by the Earth (v).

3.3.3 Background subtraction procedure

First, we estimate the non X-ray background (i,ii,iii) in the *LAC* data by using the monitor counts. The characteristics of the non X-ray background have been studied based on the dark sky and dark earth data. Among several proposed methods (Hayashida *et al.*, 1989) we here apply the technique developed by Nagoya University group. This method estimates the non X-ray background as follows ;

$$BG(\text{count/sec/channel}) = A + B \times SUD(\text{count/sec}) + C \times PIM(\text{count/sec}) \quad (3.1)$$

SUD is the *LAC* counting rate of all wires above 38keV and PIM is the counting rate of the *LAC* sense wires which are not exposed to the sky. Parameter sets (A,B,C) are determined for each of the 48 ADC channels of the TOP and MID layers.

The points of choosing this background estimation method are ;

1. The *LAC* background properties have been continuously monitored and fitted by this method. Thus we can use the best fit parameters as a function of time till the end of the mission. The effects due to long term variation of the *LAC* performance and the satellite orbits are taken into account.

2. Number of free parameters are smaller than those of other more complicated methods.

This method is known to reproduce the background within the error less than 0.2 count s^{-1} keV^{-1} in the whole energy band of the *LAC* (Yamauchi, 1991). We also checked the correctness of the Nagoya method of the non X-ray background estimation in the following three ways.

1. The dark Earth data is considered to contain only the non X-ray background. So we compared its spectrum with the model background prediction. As shown in figure 3.5, the difference between the two spectrum is less than 0.2 count/sec/keV.

2. For external X-rays, the ratio of the MID layer and the TOP layer counts should be consistent with that expected from the attenuation length of the counter Xe gas. Since subtraction of the non-X-ray background is performed for the MID and TOP layers individually, the ratio should be a good measure of the background subtraction. The MID/TOP count ratio of X-ray events should be consistent with the calculated one.

3. The sensitivity for X-rays descreases above 35 keV which corresponds to the K-edge of Xenon gas. If the energy spectrum of incoming X-rays is smooth, the count rate above 35 keV is expected to be very low. on the other hand if there remains non-X-ray badkground, the count rate spectrum becomes rather flat.

Night Earth Spectrum- calculated IBG
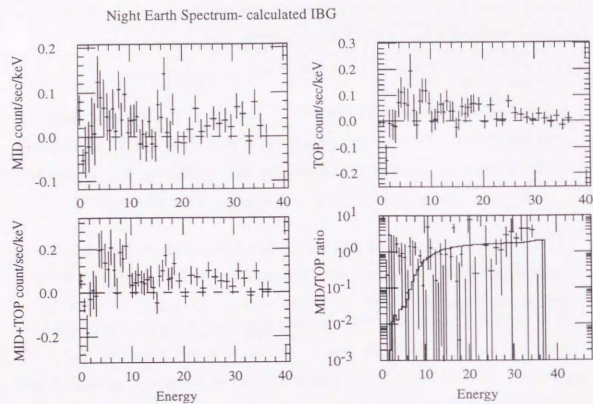
Figure 3.5: A sample of the night earth data from which the model
background has been subtracted.

We use this MID/TOP ratio as a measure of non X-ray background subtraction. If
strong point sources lies in the scan path, the PIM scaler or the SUD scaler overflows
and we can not estimate the correct background. In such case, the MID/TOP ratio of
the remaining events does not agree with the expected values for X-ray events. Two
samples are shown in figure 3.6. In the upper panel the MID/TOP ratio of the data
agree with the curve for X-ray events, and in the lower panel they do not match up
in contrast.

After subtracting the non X-ray background, there are still X-ray contamination.
Using only the data with high elevation angle between f.o.v center and the Earth
rim greater than 10 degree, solar X-ray reflection (v) is reduced to a negligible rate.
Concerning the CXB (iv), an averaged CXB spectrum observed with the *LAC* at
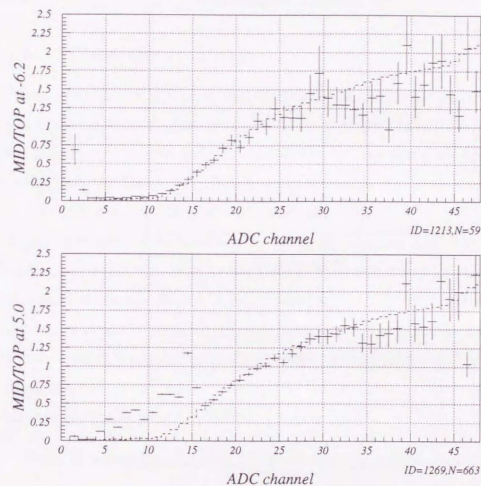
Figure 3.6: The MID/TOP ratio as a function of pulse height chan-
nel after the background subtraction, fitted by a curve
calculated for X-ray injection. The upper panel shows
data at l=-6.2 of Scan No.2, and the lower panel is at
l=5.0 in the same scan
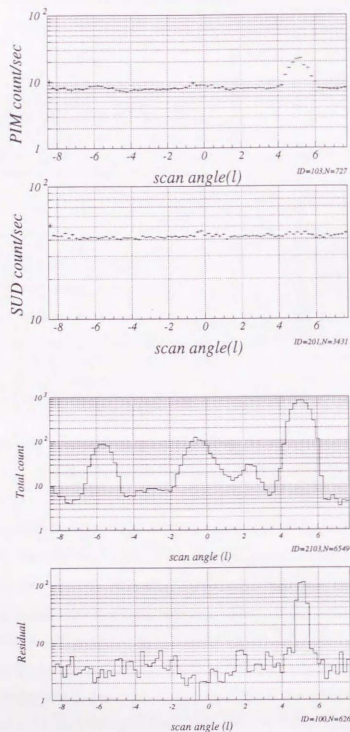
Figure 3.7: PIM,SUD,total count rate and the deviation of the MID/TOP ratio from the X-ray values in Scan No.2. At l=5, background subtraction fails due to a strong X-ray source (GX5-1)

high latitude blank sky for 142ksec is available with the accuracy less than 1.0%. This CXB spectrum is consistent with that obtained with the *HEAO A2* experiments (Yamauchi, 1991). This CXB is indeed an overestimation for this analysis because the Galactic ridge absorbs CXB. However we subtract the nominal CXB component first in this analysis and discuss this possible overestimation.

3.3.4   Fitting the scan data

We accumulate the count rate of each of the 48 ADC channels along the scan path at every $0.2°$ bin to make "scan profile" for each channel. A sample of scan profile is shown in figure 3.8. Then we have subtracted the non X-ray background and the CXB spectrum from the *Ginga* scan data as described in the previous section. For each scan, we check the correctness of the background subtraction by MID/TOP count ratio and determine the region where we use in this analysis. Plotting the residuals between the data and the model for the MID/TOP ratio as a function of scan angle, a clear dependence on the total count rate is seen (figure 3.7) because of scaler overflow. Using the value of this residual, we omit the region whose profile is not consistent with the expected X-ray count ratio in the *LAC* .

After the background subtraction and the determination of the analysis region, we fit the scan profile with the following function;

$$Total(E)(\text{count/sec}) = A(E)(1+B(E)(\theta-\theta_0))+\sum_{i=1}^{n} a_i(E)Gaussian(\theta;p_i,\sigma_i) \quad (3.2)$$

$$Gaussian(\theta;p,\sigma) = \frac{1}{\sigma\sqrt{2\pi}}\exp(-(\theta-p)^2/2\sigma^2)$$

A(E) and B(E) are constants representing the intensity and slope of the diffuse component. The direction of the line of sight of the *LAC* is shown by the angle θ along the scan path. The count rate and the position of the point source are shown by $a_i(E)$ and p_i.

Here, we simply approximate the profile of the diffuse component by one dimensional polynomial because it is expected to vary smoothly within ≤ 20 degrees from the past *EXOSAT* result(Warwick *et al.*, 1988). The intense 6.7keV iron line at the
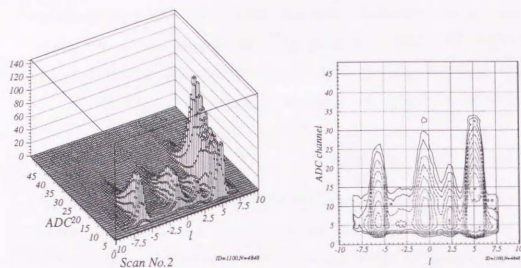
Figure 3.8: A sample of the scan profile showing l vs ADC channel
vs count/sec for the scan No.2 after the background sub-
traction;left panel is a lego plot in linear scale and right
panel is a contour plot in logarithmic scale

Galactic center region (Yamauchi *et al.*, 1990) is located in the scan path NO. 5. We
will discuss about this effects later.

The angular response of the LAC collimator is represented by the Gaussian with
σ_i fixed at a value between $0.4°$ and $0.6°$ throughout the analysis. Though the angular
response of one LAC unit has a triangular shape, we approximate the point source
structure in the scan profiles as Gaussian. The reason is that the main purpose of
the analysis here is to obtain the energy spectrum of the diffuse component, not of
the point sources with good statistical accuracy even in the high energy band.

If we use the angular response of each eight LAC unit separately, we have to treat
the scan profile of each unit individually. Furthermore each one-way scan need to be
analyzed individually because the z-axis of the satellite slightly drifted during the scan
observation. In this case the position of point sources should be represented by two
dimensional coordinates. Such a separate treatment of the data would decrease the
sensitivity to the large scale diffuse emission, because of many parameters and other
ambiguities involved. If our aim is to obtain the flux of point sources in scan paths

whose position are already known, this may be the necessary procedure. However in
this paper, the energy spectrum of the diffuse component in the high energy band is
our principal aim. With this reason, we represent the rounded angular response of
the collimator by a Gaussian function .

To determine the projected point source positions precisely, we first combine all
energy bands (1.16-18.6keV) and fit the profile with equation 3.2 by adjusting the
number of sources n and other free parameters A, B, a_i, p_i, σ_i. We stop increasing n
when reduced χ^2 of the fit no more decreases, and define the statistically significant
point source number n. Then the point source position p_i and angular width σ_i are
fixed and we fit the scan profiles for 27 energy bands with free parameters $A(E)$
,$B(E)$ and $a_i(E)$. The resultant $a_i(E)$ presents the pulse-height spectrum of $i-$th
point source and $A(E)$ and $B(E)$ indicate the energy spectrum and the slope of the
diffuse component.

Chapter 4

Hard X–ray observation by Welcome-1

4.1 Instrumentation

4.1.1 Well-type phoswich counter and pulse shape discriminator

Welcome−1 is a low-background hard X/γ–ray (60-800keV) telescope based on GSO(Ce)-/CsI(Tl) 'well-type' phoswich counters (Kamae *et al.*, 1992; Takahashi *et al.*, 1993). This 'well-type' phoswich counter uses a GSO (Gd_2SiO_5 doped with 0.5%Ce) scintillator of a size $3.4 \times 3.4 \times 1$ cm^3 for the detection part. The detection scintillator is placed at the bottom of the well-shaped CsI(Tl) shielding scintillator which works both as an active collimator and an active anti-coincidence counter.

The schematic view of *Welcome−1* is illustrated in figure 4.1. The light emitted in both scintillators are collected by a phototube optically coupled to the bottom surface of the well-shaped CsI. The light collection efficiency is higher than 90 % for the collimator part. The signal from the detection part and that from the shielding part are separated by a pulse shape discriminator (PSD). This configuration eliminates the Compton scattered γ-ray background and the internal $\beta - \gamma$ decay background very effectively. In *Welcome−1* telescope, 64 GSO(Ce)/CsI(Tl) well-type phoswich
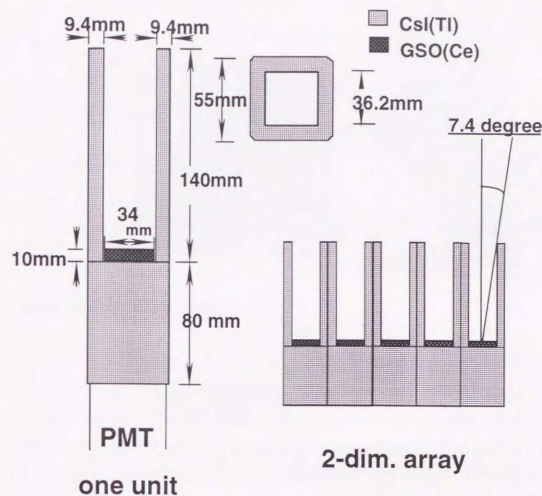
Figure 4.1: Schematic drawings of the well-type phoswich counter

counters and 36 CsI(Tl) guard anti–counters are assembled in 10×10 matrix configuration as shown in figure 4.2. This configuration enables us to use the surrounding neighbor counters as additional active shields. Signals are processed independently for 64 channels and a large area can be attained without increasing the dead time.

Let us comment about the choice of the two scintillators in our phoswich counters. The combination of the two scintillators is important for phoswich counters. The characteristics of inorganic scintillators are listed in table4.1. To discriminate the signals of two scintillators effectively, the detection part needs to have a faster decay time than the shielding part. A typical combination is NaI(Tl) for the detection part
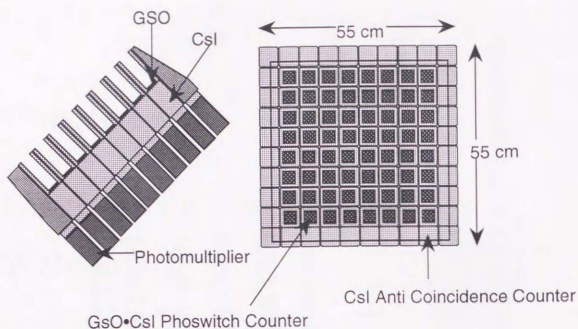
Figure 4.2: Schematic drawing of the *Welcome–1* telescope

and CsI(Tl) for the shielding part. Unfortunately NaI(Tl) has a well-known problem that long life radio isotopes are abundantly produced via neutron capture by ^{127}I. The newly developed scintillator by Hitachi Chemical GSO(Ce) is free from such a problem. It has a faster decay time (60ns) and a higher stopping power than NaI(Tl), but falls short of NaI(Tl) in the light yield.

The PSD needs to work very effectively in the well-type phoswich counters because the count ratio of the signals to the anti coincidence events is proportional to the scintillator volumes. To obtain a good S/N ratio in the lower energy region, we developed a PSD using a triple polar pulse shaping method (Murakami *et al.*, 1992). The time interval between the first and the second zero crossing in the triple polar pulse is measured by a time-to-digital converter (TDC).

A two dimensional distribution of this TDC and the pulse height is shown in figure 4.3 without applying the PSD gate. In the plot, the vertical band in the left presents clear hits on GSO(Ce) and the right band indicates events hitting CsI(Tl). Figure 4.4 show the PSD performances ; the energy spectrum (a) without PSD gate and (b)

	NaI(Tl)	CsI(Tl)	GSO(Ce)	BGO	YAlO$_3$
Effective Atomic Number	50	54	59	74	35
Density(g/cm^3)	3.7	4.5	6.7	7.1	5.5
Radiation length(cm)	2.6	1.9	1.4	1.2	2.6
Decay time(ns)	230	~1000	60	300	30
Peak emission(nm)	410	565	430	480	347
Light yield(NaI=100)	100	85	35	12	47
Index of reflection	1.85	1.80	1.9	2.15	1.94
Hydroscopic	Yes	Little	None	None	None

Table 4.1: Characteristics of inorganic scintillators

the spectrum with PSD gate. We can see in Fig.4.4(b) that events in the shielding part are suppressed and two peaks emerge with little Compton tail. This PSD is composed of four hybrid IC's and the total power consumption is 650mW/channel, suitable for use under a limited space and power consumption in balloon experiment.

4.1.2   Data acquisition system

The block diagram of *Welcome-1* 's data acquisition system is shown in figure 4.5. It consists of two sub-systems; one for the acquisition of the data from the detector and the other from star camera. Each system is constructed on VME (Versa Module Europe) bus and controlled by a 32 bit CMOS microprocessor MC68000 operated at 10MHz. The CPU is operated by a real time operating system OS-9 stored on EPROM. The operating mode and parameters in the system are controlled by ground commands received by a Data I/O module.

In the data acquisition system, controlling and processing of the data is performed by a set of processes. Four PSD gate signals from the phoswich counters are summed into a trigger signal, making a total of 16 trigger groups for 64 counters. When a trigger signal is generated in one of the 16 trigger groups and transferred into the
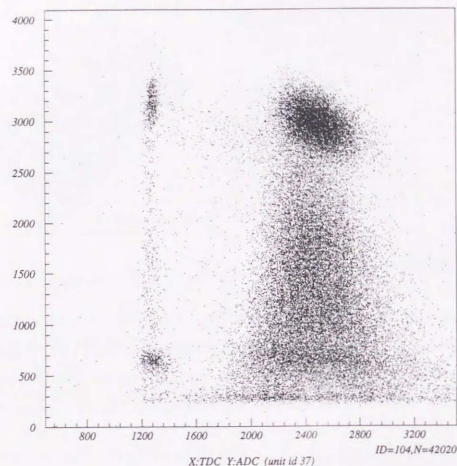
Figure 4.3: ADC vs TDC without using PSD.in the horizontal scale
1000ch corresponds to 500ns

trigger module, an interrupt routine controlled by the real time operating system
starts the data processing. The time of the trigger, ADC outputs in the particular
group, 24-bit hit pattern of the anti coincidence and 16 bit super hit pattern are
all recorded. The anti hitpattern consists of summed anti pulses from 16 trigger
groups of the phoswich counters and anti pulses from 8 surrounding anti CsI counters.
The super hit pattern consists of summed lower and upper discriminator outputs of
preamplifier pulse. Both hit patterns are used for off-line analysis. The data size
per event is 34 bytes and the monitor data size is 216 bytes. The obtained data are
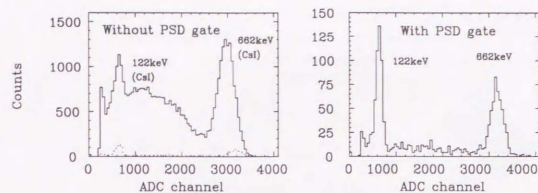
Figure 4.4: Energy spectra for ^{57}Co and ^{22}Na with/without PSD,
Using the PSD gate (right panel), the Compton tail is
suppressed effectively

recorded on a EXABYTE 8mm VCR via SCSI and also sent to the ground station
via telemetry (maximum rate 4kB/s). Under the expected trigger rate of 150Hz, all
data can be transmitted for the online analysis and monitoring.

For accurate absolute timing, we installed a quartz clock $(\Delta f/f = (2\text{-}3)\times 10^{-9})$
aboard the detector and a Rubidium clock on the ground station. The quartz clock
was calibrated by the Rubidium clock to $1\mu s$ and the Rubidium clock in turn was
calibrated to the UT time given by the GPS satellite to 2μ sec.

4.1.3 Performance

Performance of *Welcome–1* was calibrated on the ground and monitored during
the flights. The energy resolution is 28%(FWHM) at 122keV and 12%(FWHM) at
511keV. The total effective area is 740cm^2 at 122 keV and 220cm^2 at 511 keV. The
internal background energy spectrum in figure 4.6 is obtained on the ground when
the entire detector's openings were covered with 2mm thick copper and 2mm thick
lead. The peak around 368keV is due to ^{152}Gd (natural abundance= 0.2%, half life
$= 1.1\times 10^{14}$y, E_α=2.14MeV) and the broad enhancement around 1 MeV is due to the
radio active contamination of the Th and U series in GSO. The counting rate of the
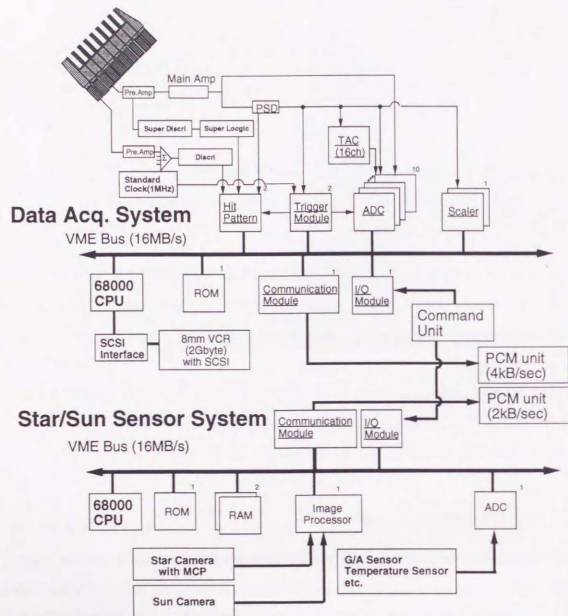
Figure 4.5: Schematic drawing of Welcome-1 data acquisition system
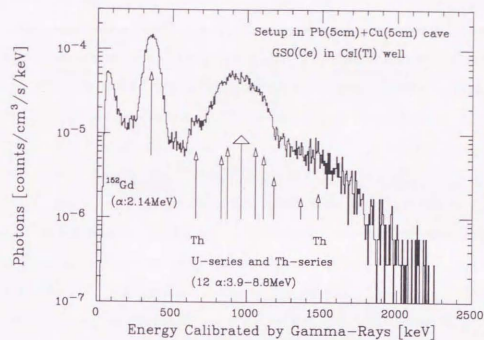
Figure 4.6: The internal background spectrum

368keV peak is 0.181 ± 0.002 count/sec/channel. The field of view (FOV) is mainly determined by the depth of the CsI(Tl) well, and the angular response is measured on the ground calibration to be $15.4°$ (FWHM) at 122 keV and $18.2°$ (FWHM) at 511 keV. This measured angular response and calculated one by a Monte-Carlo simulation (EGS4) is compared in figure 4.7. This agreement shows that the systematic error of the calculated detector response is less than 3 %.

Figure 4.8 shows the background energy spectrum obtained during a balloon flight at an altitude 38km. The spectrum is well represented by the sum of the internal background shown in figure 4.6 and the atmospheric hard X-ray/γ-rays estimated by a Monte Carlo simulation based on data taken in a balloon flight (Miyazaki, 1993). This result shows that the internal background during balloon flights is about the same level as that on the ground.
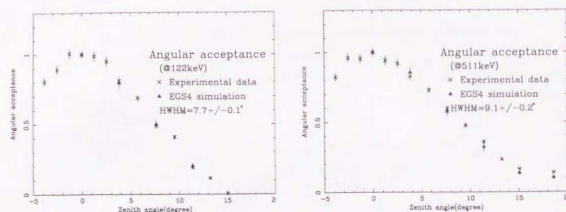
Figure 4.7: The measured and calculated FOV for 122keV and 511keV
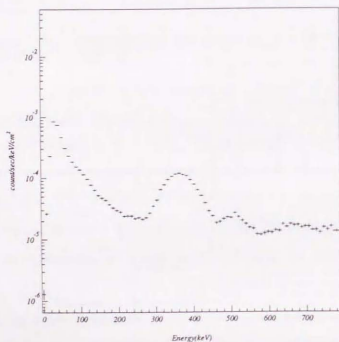
Figure 4.8: The background spectrum obtained during the balloon
flight at an altitude of 38km

4.1.4   Attitude control/monitoring system

The elevation angle of the detector is moved by the elevation angle motor which is controlled by the command from the ground station (see figure 4.9). The elevation angle is measured by two slope gauges during the observation within a 1.0 degree accuracy. The azimuthal angle of the gondola is changed with the azimuthal control motor and the geomagnetic sensor (GA sensor) by the "Yorimodoshi" method. The azimuth control motor applies torque to the gondola by twisting the rope between the balloon and the gondola. The motor rotates the gondola until the output voltage of the GA sensor becomes zero. The GA sensor is set on a turn table which can be rotated via the command from the ground station. So the azimuthal angle of the detector is controlled by rotating the turn table of the GA sensor. The azimuthal angle is measured by a spare GA sensor on the gondola. This azimuth and elevation control technique was established by ISAS balloon group (Hirosawa *et al.*, 1971).

For the *Welcome–1* experiment, we developed a new star camera / sun camera system to monitor the attitude of the detector. The declination angle of the geomagnetic field in Brazil is as large as 20 degrees and is expected to change during the flight. So it is difficult to determine the attitude of the detector precisely only by geomagnetic sensors. The star camera consists of a micro channel plate and a CCD camera. It has a field of view $9.1° \times 6.3°$. The sun camera consists of a wide view lens with a dark filter and a CCD camera having a field of view of $130° \times 130°$. Both camera are mounted in parallel to the detector's line of view.

Image of the star/sun camera is processed by a computer system based on a VME bus (see figure 4.5). Both signals from the star/sun camera are fed into a video processor. In the image, bright pixels above a given threshold level are selected. The position and the brightness of the pixels are sent to the ground station via telemetry of 16kbps. The average time to send an image is about 2 seconds . On the ground station, the image is reconstructed and displayed in real time. We can send the control command to the gondola by monitoring the image of the sun/star camera. The azimuthal and elevation angle can be determined to 0.2 ° accuracy by off-line analysis.
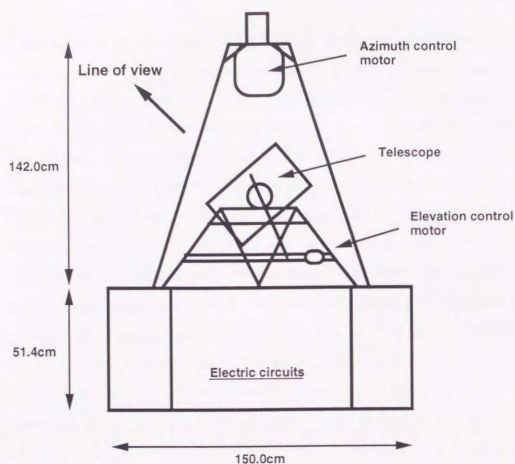
Figure 4.9: Schematic drawing of the Welcome-1 detector and the gondola

4.2   Observation

The Welcome–1 telescope was launched at 04:57 (Brazil local time, hereafter referred as BLT, a time difference between UT and BLT is −2 hour) in 1991 December 3, from the balloon base of INPE (INstitute de Pesquisas Espacicis,Brazil) at Cachoera Paulista, states of Sao Paulo, Brazil (S22°39′44″, W45°00′44″) with a 250000m³ hydrogen balloon. The detector reached at the ceiling altitude 36.9km about two hours after the launch. The detector was cut from the balloon at 15:01 and was recovered at 250km west of the ground station. During the level flight, the balloon altitude was kept at 4.43 ± 0.05g/cm² . The flight route of the balloon was plotted on the figure 4.10.

The telescope's elevation angle was fixed at $69.0°\pm0.05°$ due to a technical problem in the control system at 09:00. The azimuthal control worked successfully and the pointing direction of the telescope was monitored by a GA sensor and a Sun camera to 0.2° accuracy.

The detector observed Centaurs A from 09:10 to 11:10. Then the detector's azimuthal angle was fixed to 180° to scan the off-Galactic plane region from 11:41 to 12:08. Next the azimuthal angle was fixed to 211° to scan the Galactic Center region (hereafter referred to as the GC scan) from 12:08 to 12:30. The field of view of the detector is shown in figure 4.11. After the GC scan, a galactic plane region at about l=345° was observed from 12:35 to 14:05 by alternatively pointing at the source (on-source observation) and at the blank sky background (off-source observation). During the observation, the atmospheric depth was kept constant and the telescope's FOV scanned the sky regions as shown in figure 4.12. The total observation time was 42 minutes for the Galactic plane and 22 minutes for the GC scan.

After the Galactic plane observation, we rotated the detector around the azimuthal direction to calibrate the alignment of the sun camera and the detector. And we also calibrated the the the output of the GA sensor and by the sun camera. Fortunately, a hard X-ray emitting solar flare occured at 16:33 UT (corresponding to 14:33 in BLT) (Kosugi et al., 1992). At that time, the balloon was flying at a longitude W47°51′ and a latitude S22°40′. The sun was located at an azimuthal angle 87.05° and an elevation angle 68.9°.

The hard X-rays above 50 keV was observed by HXT on board YOHKOH satellite (Ogawara et al., 1992; Kosugi et al., 1992) and γ ray up to 10MeV was observed by GRS (Yoshimori et al., 1992). So we could confirm that the detector and the sun camera looked at the sun at the same time.
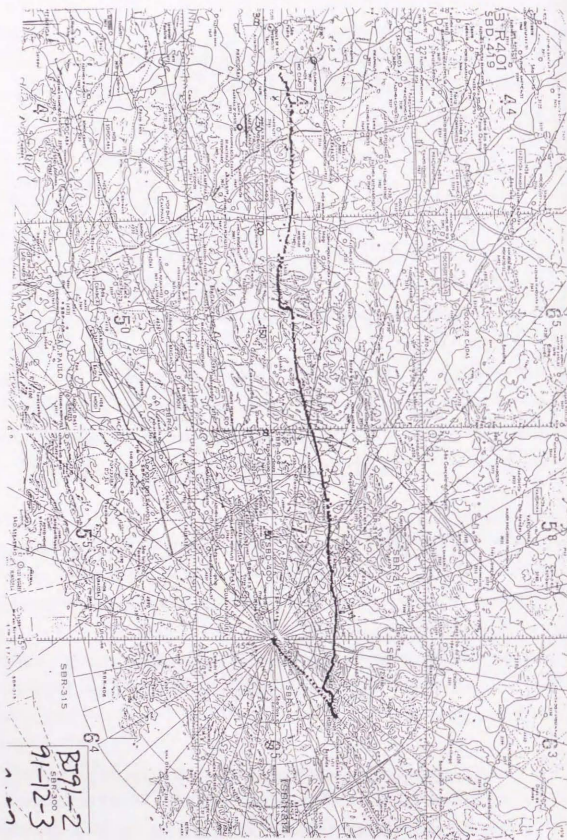
Figure 4.10: The flight route of the Welcome-1 on 3 Dec. 1991
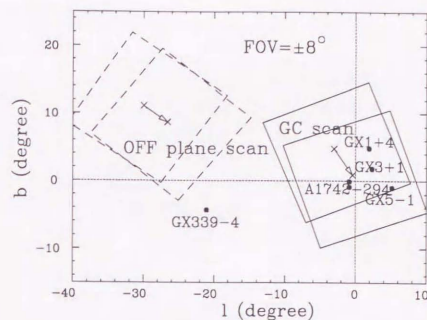
Figure 4.11: The filed of view of the detector during the GC scan observation and known hard-Xray sources

4.3   Data Analysis

4.3.1   Gain correction

The gain correction is necessary to obtain the correct energy scale. The gain is different among the 64 phoswich counters, and it changes during the observation due to the temperature drift of scintillators (-0.5%/degree) and also by the change of the detector orientation relative to the Earth geomagnetic field. The spectral peak around 368keV produced by the ^{152}Gd contamination in GSO scintillator is used as an energy calibrator. The energy spectrum of each counter is integrated for overlapping 30 minute intervals, and the fitting of the 368 keV peak by a Gaussian gives gain correction factor as a function of time. After applying this gain correction, the spectral peak from the 64 well-type counters are aligned in 1500 ADC channels within the rms error of 0.22 % (figure 4.13). The time variation of the gain is also corrected for within the rms error of 0.25 % as shown in figure 4.14.
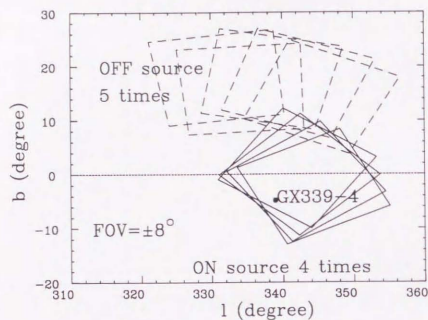
Figure 4.12: The field of view of the detector during the Galactic plane observation and known hard X-ray source GX339-4
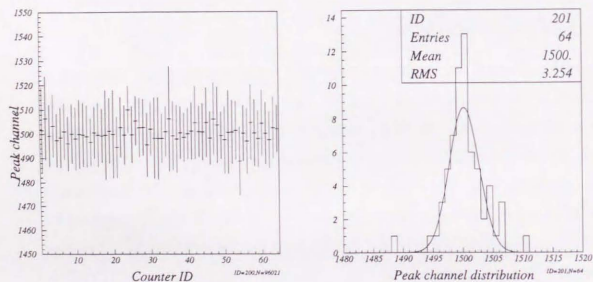
Figure 4.13: Peak channels of ^{152}Gd contamination for 64 phoswich counters after the gain correction.
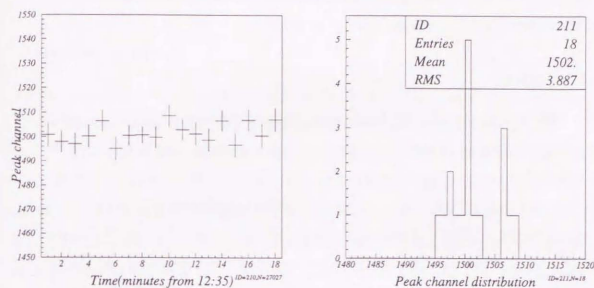
Figure 4.14: Time variability of peak channels of ^{152}Gd contamination after the gain correction.

4.3.2 Event selection

To reduce the background events produced by Compton scattering and $\beta - \gamma$ decays , the PSD circuit in the on-board system rejects GSO events which accompany some γ-ray energy deposited in CsI(Tl) in the same phoswich counter. Though there are still background events caused by Compton scattered photons that deposit the remaining energy in the neighboring counter, charged particles and atmospheric γ-rays from the detector opening angle can be effectively removed.

In the off-line analysis, we look into the data recorded on VCR and select good events based on the following information; 1)Event multiplicity, 2)Anti hitpattern, 3)Super hitpattern and 4)Event time interval. Each item is explained here in some detail.

Event multiplicity

As described in section 4.1, 64 PSD gates from the phoswich counters are grouped into 16 trigger signals. For one trigger, four ADC outputs are therefore recorded. If two or more ADC outputs exceed the event threshold level ($\sim$ 20keV), we reject both

events because they are likely to originate from one Compton scattering. About 25 % of the recorded GSO events are rejected in this step.

Anti hitpattern

In the PSD circuit, the 16 anti signals each comprising events from four phoswich counters go through an ORgate and form an ORed anti signal. The signals from the 36 anti counters surrounding the detector are amplified into bipolar pulses. They are combined into eight groups and an energy discriminator generates an anti pulse with the threshold set to 70 keV. These $16 + 8$ anti pulses form a 24 bit anti hitpattern. Using the flight data we study correlation between each GSO event and its simultaneous hitpattern and define a mask hitpattern for each counter. This is essentially a map of significant coincidence among the detectors. A 37 % of the recorded events is removed using the anti hitpattern. The energy spectrum of rejected events in this step is shown in the right upper panel in figure 4.15. The events around 368keV which are created in GSO remain, but the peak at 511keV due to positron annihilation is removed. This shows that Compton scattered events are suppressed effectively.

Super hitpattern

When the incident γ-ray or charged particles deposit an energy in excess of 850 keV, a pulse shape may be distorted due to the saturation in the amplifiers. If the pulse shape accidentally meets the PSD window, a fake event occurs.

To cope with these events, the trigger pulse is inhibited for 300μsec on board. However if the energy deposited in CsI scintillator becomes larger than 60MeV, the analog system is affected for a period comparable to the longest after glow ($\sim$ 1msec) in CsI. To avoid the effect of after glow, a negative and an extra positive discriminator for the preamplifier outputs generate a super lower/upper pulse for as long as 420~900 μsec. The level of this super upper discriminator is several times higher than the nominal upper level. These super pulses from combination of four phoswich counters are ORed and recorded as a 16 bit super hitpattern. Using the super hitpattern, 60% of the recorded events whose spectrum is shown in the lower left panel of figure 4.15

is rejected.

Event time interval

A fake event caused by a huge energy deposit in CsI scintillator lasts longer for larger energy deposit. Some of the fake events lasting more than 800 μsec are not rejected by the super hitpattern. Such fake events tend to occur successively, but the time intervals for celestial γ ray events with Poisson probability distribution should follow an exponential function. Based on this, we reject events if the time interval between selected events is shorter than 1ms. After this time interval selection, we obtain the energy spectrum shown in the lower right panel in figure 4.15 with their time interval distribution in figure 4.16. The survivors are 13 % of the initially recorded events. The average background level is as low as a few times 10^{-6} counts cm^{-2}sec^{-1}keV^{-1}. Then we subtract the events obtained in the off-source sky from these on-source data, after both data are cleaned in this way to suppress the internal and atmospheric backgrounds.

4.3.3   Detection efficiency

For the first step to determine the detection efficiency, we calculate the absorption of γ-rays before entering the detector. The γ-rays are attenuated by the 4.43g/cm^{2}of the air, by the covering aluminum sheet and by BaSO$_4$ light reflection powder painted on GSO scintillator. The systematic error of the estimated attenuation factor is about 2% for the Air, 2% for Al and 10% for BaSO$_4$. They are summarized in the left panel of figure 4.17.

Next, we estimate the quantum efficiency and the angular response of GSO scintillator by a Monte-Carlo simulation. The systematic error is considered to be 3%. The quantum efficiency is, in reality, described by two-dimensional matrix elements whose one axis is input photon energy and another axis is output photon energy. After the data selection, however, Compton scattering is suppressed and the matrix is composed of mostly diagonal elements as shown in figure 4.19. As our purpose is
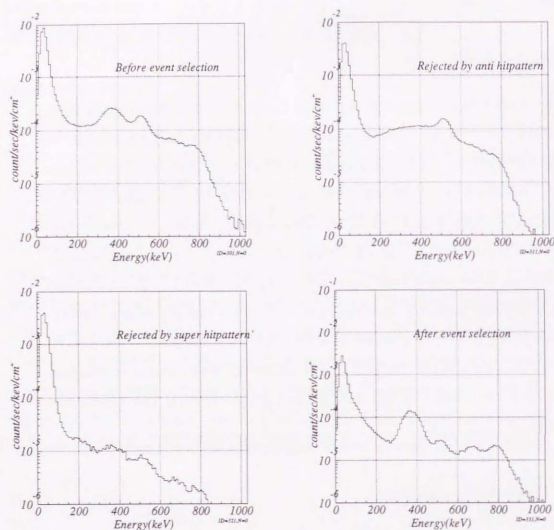
Figure 4.15: Energy spectra of before and after the event selection and
those of rejected events.

not the study of line emission narrower than the detector resolution, we simplify the
quantum efficiency as one dimensional efficiency.

The trigger efficiency of PSD gate for low energy γ-rays is monitored by 16 TDCs
during the observation. Using 2-dimensional TDC vs ADC plots (a sample is shown
in figure 4.18), we fitted the TDC distribution for γ-rays by a Gaussian function
which is truncated to zero above a certain channel and calculated the fraction of the
cut-off area. The systematic error is about 10% at 60keV.

The dead times caused by the detector electronics, the data acquisitions and the
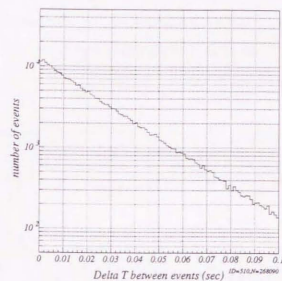
Figure 4.16: Distribution of the time interval between selected events
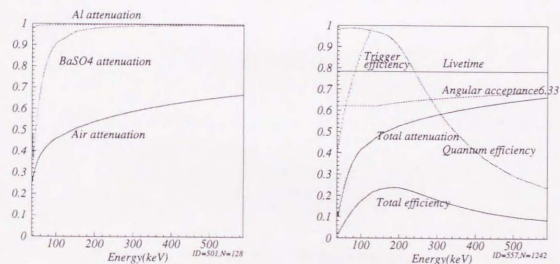
Figure 4.17: Detection efficiency of the *Welcome-1*

event selection are estimated from pseudo-events which are artificially generated on board. Counting the survived pseudo events after the event selection, the dead time becomes 22±1%. The total detection efficiency for GX339-4 observation is shown in the right panel of figure 4.17. The parameters for the efficiency calculation are precisely calibrated from the Crab nebula observation and agree well with those of previous observations (Miyazaki, 1993; Tamura, 1993).
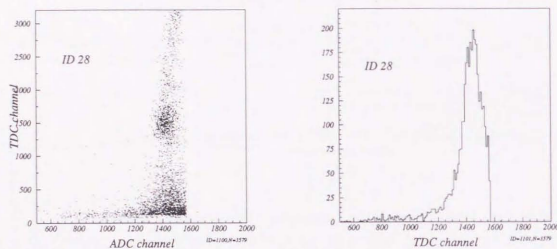
Figure 4.18: A sample of ADC-TDC plot and TDC distribution during the observation
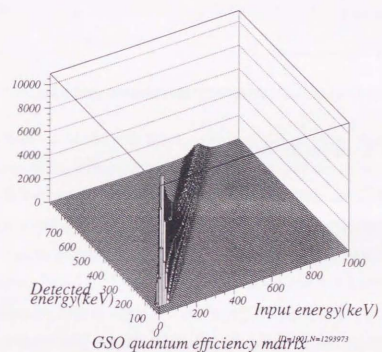
Figure 4.19: 2-dimensional quantum efficiency matrix of GSO, vertical scale is arbitrary.

Chapter 5

Results

5.1 Results from Ginga scan observation

5.1.1 Results from scan fitting

In analyzing the *LAC* scan data with the method described in chapter 3, we first check the gain correction based on the 22.1 keV line. We subtract both the non X-ray background estimated base on the SUD and PIM monitor counts and the nominal cosmic X-ray background as described in section 3.3.3. The MID/TOP ratio profile is then monitored as figure 3.7. Based on this MID/TOP ratio profile, we analyze only the X–ray data where the subtraction gives reasonable results. The number of point sources are estimated from the count rate profile between 2.3 keV and 18.6 keV, and finally the overall scan fitting is carried out using the scan profile of 27 energy band individually. This procedure detects point sources with an intensity down to about 0.3 mCrab. This is close to the level limited by the beam-to-beam fluctuation of the CXB (Hayashida *et al.*, 1989). The reliability of the scan fitting method is discussed later in this chapter. The parameters for each scan fitting are summarized in table 5.1.

The scan profiles and results from scan fitting are shown in figure 5.1 through 5.6. The upper left panel in each figure shows the scan profile where the count rate between 2.3 keV and 18.6 keV after non X-ray and cosmic X-ray background subtraction is

Scan No.	pathname	l	b	point sources	diffuse component	figure No.
1	890406	$-7.5 \sim 7.5$	$1.6 \sim 2.5$	7	constant	Fig. 5.1
2	890403	$-8.1 \sim 4.1$	$-1.5 \sim -0.5$	7	constant	Fig. 5.1
3	890407	$-7.5 \sim 2.9$	$-2.3 \sim -1.7$	7	constant	Fig. 5.3
4	890410	$-4.1 \sim 3.9$	$-9.9 \sim -9.4$	4	constant	Fig. 5.4
5	880317	$-14.7 \sim -7.5$	$0.3 \sim 0.4$	5	constant	Fig. 5.5
6	871010	$20.5 \sim 37.5$ averaged at 30.0	$-0.7 \sim -0.1$	9	longitude dependent	Fig. 5.6

Table 5.1: Summary of scan fitting parameters; selected region and

plotted as a function of the scan angle. The upper right panel shows the obtained energy spectrum of the diffuse component and lower panels are those of point sources.

In the scan No.6, the scan profile in figure 5.6 clearly shows that the diffuse component depends on the Galactic longitude. To describe this spatial structure, we treated B(E) in equation 3.2 as a free parameter, where θ_0 was fixed at 30°. So A(E) corresponds to the diffuse component averaged at $l =30°$ and B(E) is the slope of intensity along the Galactic equator. The resultant value of B(E) is about 5% per degree. In the other scan fitting, we fixed B(E) = 0 at any energy and at any point because the slope is less than 2% degree^{-1}. In scan No.4 running at b∼9.5 ° in the figure 5.4, we obtain only upper limit above 4keV for the diffuse component. In the lower right panel of figure 5.4, upper limit of 3 σ confidence level is shown.

5.1.2 Point sources

In the scan fitting, we also obtain the energy spectra of point sources. The accuracy of position determination is 0.1∼ 0.2 degree considering the possible miss detection of faint neighboring sources as well as the satellite attitude stability during the observations. Using *Einstein* IPC data (Einstein Catalog Committee, 1990) and combined
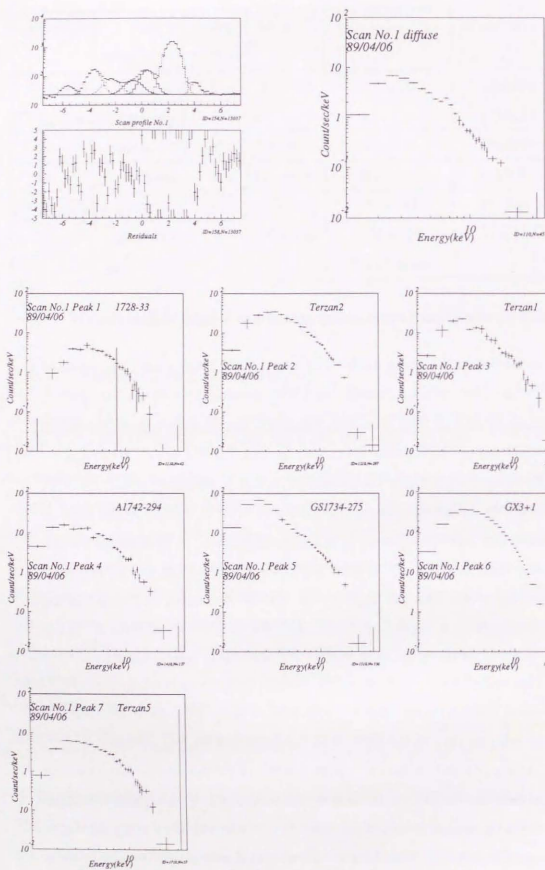
Figure 5.1: Results of Scan fitting No.1
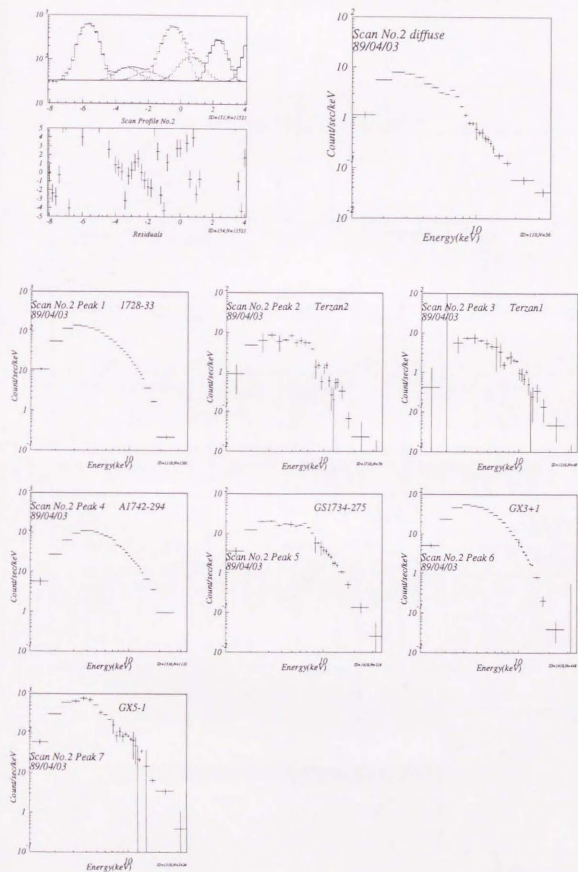
Figure 5.2: Results of Scan fitting No.2
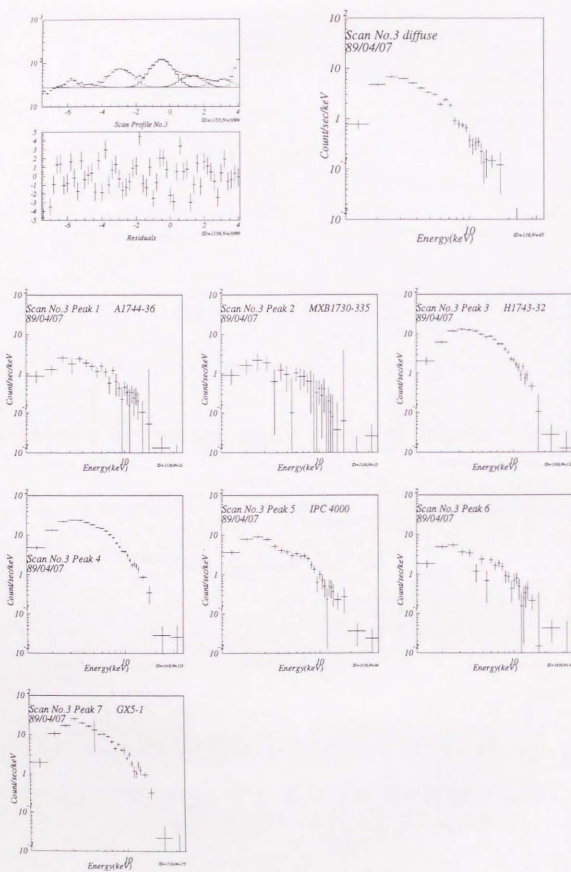
Figure 5.3: Results of Scan fitting No.3
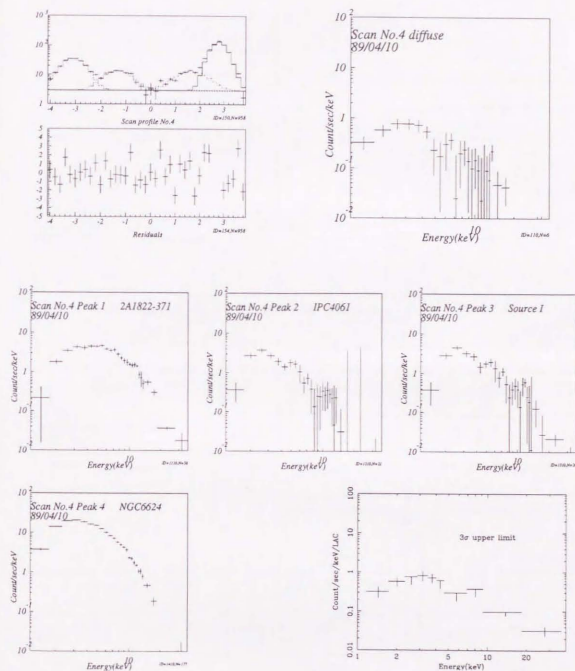
Figure 5.4: Results of Scan fitting No.4
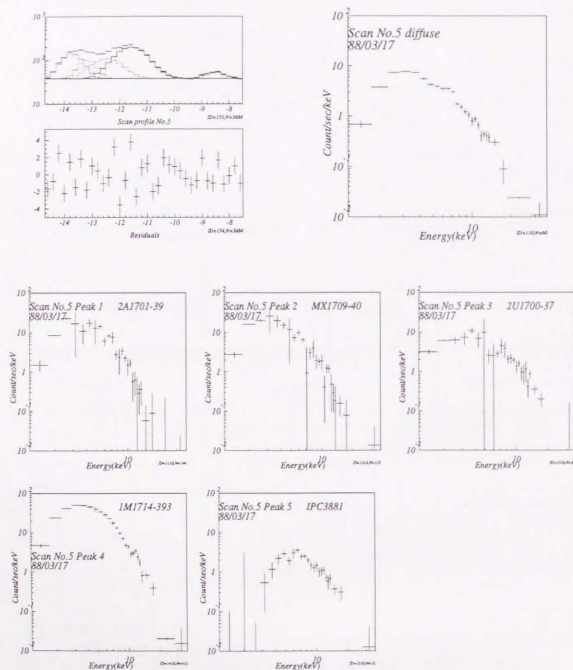
Figure 5.5: Results of Scan fitting No.5
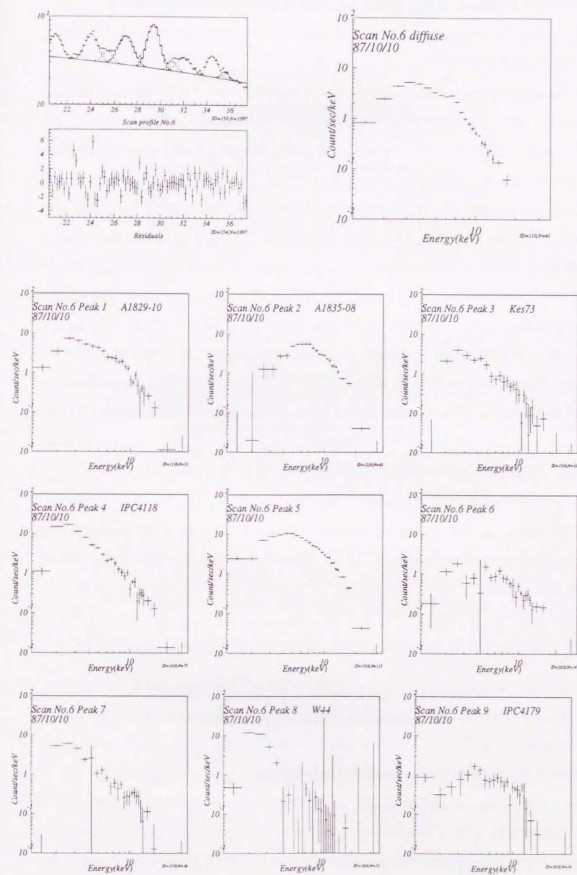
Figure 5.6: Results of Scan fitting No.6

X-ray catalog by Dolan (1983) whose positions is more accurate than 4U or 2A cata-
logues, most of the sources match up with known X-ray sources (Figure 5.7 and 5.8).
They are summarized in table 5.2.

As the source position perpendicular to the scan path can not be determined from
the present data alone, identification of sources needs to be carefully checked. We
derive tentative flux of each X-ray source assuming the identifications are all correct.
Since the angular response is almost independent of X-ray energy, hardness ratios are
useful to confirm the source identification. For example, the energy spectrum of a
low-mass X-ray binary GX3+1 (figure 5.1) obtained in Scan No.1 is well represented
by a (disk blackbody + blackbody + broad line) model, not by a single disk blackbody
model or by a single blackbody model (see table 5.3), in agreement with the results
from a pointing observation by the LAC (Makishima et $al.$, 1989). In the present
study, the hardness ratio is defined as Count(6.33-16.1keV)/Count(3.45-6.33keV),
and the softness ratio as Count(1.15-3.45keV)/Count(3.45-6.33keV). These ratios are
plotted in figure 5.9. The consistency has been checked by the sources scanned more
than once in the observation. For example, the ratios for GX3+1 obtained in scan
No.1 and No.2 agree well within 3 sigma level.

Most of the point sources identified are low mass X-ray binaries which cluster in
down left quarter in the color-color diagram, figure 5.9. The upper left population is
a group of soft sources such as an SNR Kes 73 and the down right population is hard
sources like pulsars.

5.1.3 Reliability of the extraction of diffuse component

The reliability of the energy spectrum of the ridge emission obtained from the scan-
profile fitting needs to be studied. There are two aspects which may cause error in
the resultant spectrum; one is the systematic error in the background subtraction and
the other is the error in the point source subtraction.

The errors in the estimation of non X-ray background are less than 0.2 count $\sec^{-1}$
keV^{-1} (Yamauchi, 1991). This has been confirmed by applying the same technique to
the night earth data as described in Chapter 3 (see figure 3.5). The correctness of the
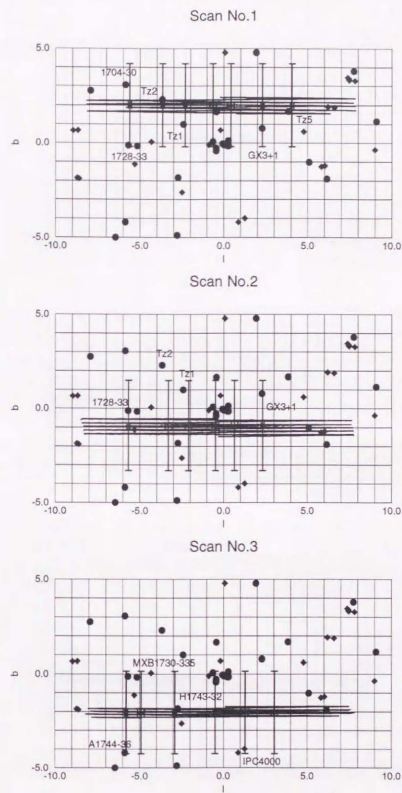
Figure 5.7: Source identification Scan No.1,2,3

Scan No.4
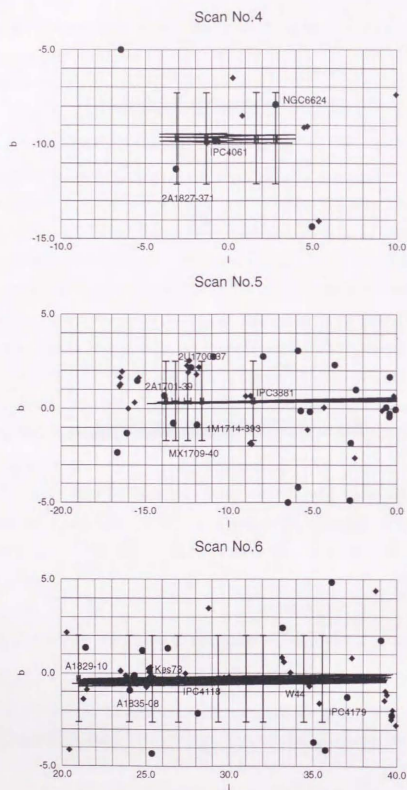
Scan No.5

Scan No.6

Figure 5.8: Source identification Scan No.4,5,6

Scan	No.	l	Tentative ID	Intensity(counts/sec)		
				1.15-3.45keV	3.45-6.33keV	6.33-16.1keV
1	1	−5.6±0.1	1728-33	3.7±0.3	11.0±0.7	10.1±0.5
	2	−3.7±0.1	Terzan2	48.8±1.6	67.4±6.2	54.4±0.6
	3	−2.3±0.1	Terzan1	31.6±1.7	37.7±4.4	17.0±0.5
	4	−0.6±0.2	A1742-294?	27.6±0.9	32.6±2.3	23.5±0.6
	5	0.4 ±0.2	GS1734-275?	106.9±1.0	50.8±0.8	31.9±0.8
	6	2.3 ±0.1	GX3+1	524.8±1.2	859.3±1.5	456.8±1.1
	7	4.1 ±0.1	Terzan5	10.0±0.3	12.4±0.4	10.7±0.4
2	1	−5.6±0.1	1728-33	187.2±0.8	302.8±0.8	205.8±0.6
	2	−3.3±0.2	Terzan2?	14.9 ±2.4	23.1±1.3	18.0±1.6
	3	−2.1±0.2	Terzan1?	6.3±4.9	13.5±0.8	10.0±0.8
	4	−0.4±0.2	A1742-294?	109.3±0.9	277.9±1.9	247.1±4.4
	5	0.6 ±0.2	GS1734-275?	33.8±1.2	53.9±1.6	52.5±0.8
	6	2.3 ±0.1	GX3+1	75.1±0.5	118.4±0.6	65.3±0.4
	7	undetermined	GX5-1	919.4±9.0	1632.6±13.6	1713.2±14.0
3	1	−5.8±0.1	A1744-36?	4.1±0.5	4.1±0.5	3.4±0.5
	2	−4.9±0.1	MXB1730-335	3.8±0.8	2.0±0.7	<2.3
	3	−2.9±0.1	H1743-32	19.2±0.9	29.2±0.9	22.0±0.9
	4	−0.5±0.1		37.5±0.9	53.0±1.2	37.6±1.2
	5	1.3 ±0.2	IPC4000	16.2±0.8	11.1±0.8	9.0±1.1
	6	3.0 ±0.2		9.1±0.7	<5.7	5.7±0.8
	7	undetermined	GX5-1			
4	1	−3.1±0.1	2A1822-371	5.5±0.4	12.8±0.6	16.9±0.8
	2	−1.3±0.1	IPC4061	5.3±0.5	4.9±0.7	3.8±0.9
	3	1.7±0.1	Source I(Yamauchi, 1991)	4.3±0.4	6.4±0.6	5.6±0.8
	4	2.8±0.1	NGC6624	35.1±0.4	41.5±1.0	28.4±0.8
5	1	−13.8±0.1	2A1701-39	18.2±5.3	54.5±4.5	26.3±4.8
	2	−13.2±0.2	MX1709-40	35.2±9.5	22.2±3.5	8.6±4.0
	3	−12.5±0.2	2U1700-37?	25.7±	11.6±1.3	11.9±1.2
	4	−11.6±0.1	1M1714-393?	68.8±1.2	115.7±1.8	56.9±1.4
	5	−8.5±0.1	IPC3881	<0.2	6.0±0.9	12.1±0.7
6	1	21.0±0.1	A1829-10	11.4±0.7	11.4±0.7	7.8±0.8
	2	24.0±0.1	A1835-08(SctX-1?)	1.6±0.5	12.6±0.5	22.2±0.5
	3	25.4±0.2	Kes73	5.8±0.4	3.6±0.6	2.5±0.4
	4	27.0±0.1	IPC4118	27.8±0.6	13.0±0.5	5.9±0.6
	5	29.4±0.1		11.0±0.4	27.5±0.5	27.2±0.4
	6	31.0±0.2		2.8±0.4	3.6±0.4	3.6±0.4
	7	32.0±0.2		10.0±0.4	2.8±0.4	2.3±0.3
	8	34.5±0.1	W44	18.5±0.3	<1.6	<1.1
	9	35.6±0.1	IPC4179	<1.2	3.1±0.8	3.9±0.4

Table 5.2: Point sources obtained in scan fittings.Intensities are not
corrected for the collimator response.1 Crab flux gives
roughly 10^4 counts s^{-1} in 1∼6 keV

Blackbody

absorption	N_H 10^{22} cm^{-2}	0.0
blackbody	temperature(kT)	1.45 ± 0.02
	normalization	230.3 ± 0.3
χ^2/d.o.f	$6260/17=268.3$	

Disk blackbody

absorption	N_H $(10^{22}$cm$^{-2})$	1.39 ± 0.01
disk blackbody	temperature(kT)	2.22 ± 0.09
	normalization	5199.0 ± 109.0
χ^2/d.o.f	$375.2/17=22.07$	

Disk blackbody+blackbody + broad line

absorption	N_H $(10^{22}$ cm$^{-2})$	1.44 ± 0.07
disk blackbody	temperature(kT)	1.74 ± 0.02
	normalization	$(1.09 \pm0.02) \times10^5$
blackbody	temperature(kT)	2.40 ± 0.10
	normalization	74.7 ± 4.5
Gaussian	center energy	6.52 ± 0.11
	sigma	0.81 ± 0.17
	equivalent width	222 ± 51
χ^2/d.o.f	$12.03/12=1.00$	

Table 5.3: Parameters of GX3+1 energy spectrum fit

background subtraction can be checked from the off-plane (b∼-9.5) scan observation No.4. The fitting gives only an upper limit above 4 keV for the ridge emission as shown in figure 5.4. It is natural to assume that the diffuse emission becomes very weak at such a high latitude, therefore this result is consistent with the expectation.
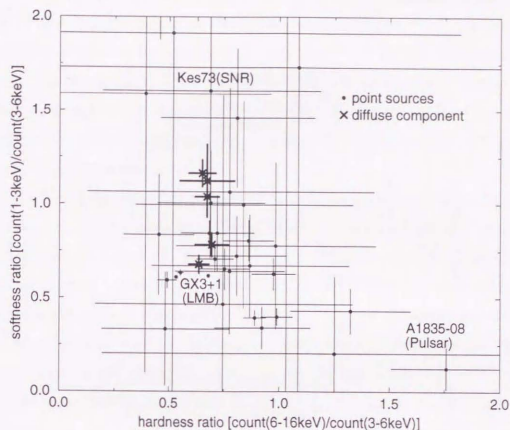
Figure 5.9: Color-color diagram of point sources and diffuse component

The error of the total background (CXB + non X-ray) subtraction above 4keV is less than about 0.2 count sec^{-1} keV^{-1}.

As explained in Chapter 3, we have subtracted the CXB spectrum from the scanning data . This CXB spectrum was an average over 142 ksec of the LAC observation at high latitude where the attenuation by the interstellar matter is negligible. In the low energy band (∼ several keV), the flux of obtained diffuse emission is a few times higher than the CXB spectrum. The absorption of CXB would change the ridge emission below 3 keV by about 10 %. The flux of the ridge emission is comparable to CXB in the high energy band as shown in figure 5.10. However, we used the CXB spectrum averaged over more than 10 times longer observations than the scan observation. So it is unlikely that the ridge emission significantly suffers from the errors

in the CXB subtraction.
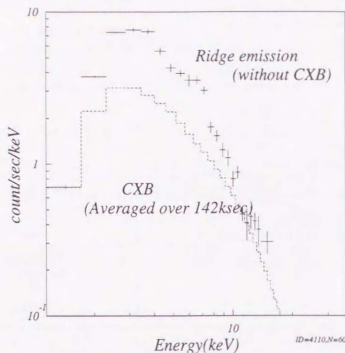
Figure 5.10: Energy spectra of the ridge emission and CXB

The pulse-height spectra of the ridge emission in figure 5.1 - 5.6 shows smooth feature except for iron emission line. Yamauchi (1991) studies the ridge emission between 1.5 and 11 keV by selecting sky regions where no cataloged X-ray sources exist. Averaging the equivalent width of the iron line emission from the five sky regions including our scan No.1, he obtains 715±196 eV. This is consistent with the result of our scan fitting spectrum which shows 643 ± 118 eV. In scan No.3, the average value by Yamauchi (1991) for three pointing is 774±192 eV, also consistent with the present value of 544 ±230 eV from the scan fitting. This supports the reliability of the present results. In the energy spectra of known low-mass binary X-ray sources whose observed intensity is comparable to the ridge emission (for example, Terzan 1,Terzan 2,Terzan 5 in the Scan no.1 , H1743-32, GX5-1 in the Scan no.3 and NGC6624 in the Scan no.4), there seems no significant iron line emission in contrast.

To confirm that photon assignment between the diffuse component and the point sources is correctly performed in the scan fitting, we analyze again the dataset of scan No.4 without subtracting the nominal CXB energy spectrum and check if the diffuse spectrum thus obtained agrees with that of the CXB. The resultant spectrum of the diffuse component is shown in figure 5.11. It agrees well with the expected averaged CXB spectrum as shown in figure 5.11, supporting the correctness of dividing the spectrum of the diffuse component.

The residual of the CXB fit to the scan No.4 can be used to estimate the systematic error in this analysis. As shown later, the contribution from the diffuse ridge emission is estimated to be at most 2% of the CXB flux at $b = 9.5°$. Therefore, the upper limit to the diffuse flux in scan No.4 indicate the systematic effect caused by the point source subtraction and the background uncertainty. The residual spectrum between 7 keV and 18 keV has been fitted with a power-law model of photon index 2.3, which is the best fit index for the overall ridge spectrum described later. The 90 % upper limit of the normalization is 15 photons cm^{-2} sec^{-1} keV^{-1} at 1keV. This is about 10% of the average flux of the ridge emission and can be taken as a practical measure of the systematic error in the present analysis.

5.1.4   Energy spectra of the diffuse component

The six energy spectra of the diffuse Galactic ridge emission are shown in figure 5.1 through 5.6. In this section, we will look for the spectral feature by several model fittings. Hereafter we mainly use XSPEC 8.41 for the spectral fit (Shafer et al., 1992; Shafer et al., 1994) and the errors show 90 % confidence level for a single parameter. To eliminate the effects of the uncertainty in N_H and the contribution from a possible soft component, we first analyze the data between 4 keV and 16 keV, where the CXB contamination is also negligible.

Since strong iron emission line is seen in the energy spectra for scan No.1,2,3,5, and 6, the existence of the hot gas is almost obvious. We first fit the spectra by an absorbed thin thermal bremsstrahlung plus a Gaussian iron emission line model. The best fir parameters are listed in table 5.4. First, we look at the common features in
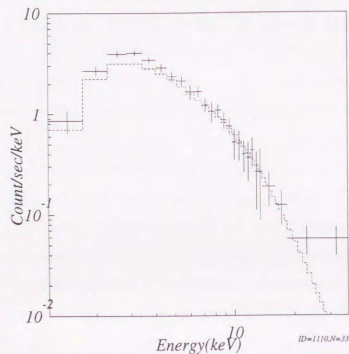
Figure 5.11: Reproducibility of a diffuse component by the scan fit-
ting, dashed histogram is the expected CXB energy spec-
trum and crosses are the result obtained by scan fitting

the energy spectra. The absorption column density become zero for all spectra and
the electron temperature of the continuum emission varies from 6.3 to 10.3 keV. The
center energy of the line is consistent with 6.7 keV (He-like ion) and the line width
agrees with the instrumental resolution except for scan No.6 which exhibits a line
centered at 6.60 ± 0.06keV and an intrinsic σ of 0.25 ± 0.1 keV. The equivalent width
of the line ranges from 500 to 1000 eV.

We note that this model fit is not statistically acceptable at 90 % confidence
level (Bevington and Robinson, 1992) mainly because the data exceed the thermal
bremsstrahlung model in the high energy band. Furthermore, the total absence of
the absorption column density is unreasonable for the ridge emission. The spectral
fit here is performed only above 4keV, however one should be capable of detecting

N_H around 3×10^{22} cm^{-2}.

The energy spectrum of the scan No.2 shows the most strong iron line emission.
This path includes the iron line emitting region of $1.8°\times 1.0°$ at the Galactic center
reported by Koyama et al. (1989). Since we model the scan profile by a sum of a
uniform diffuse component and several point sources, the diffuse component obtained
in the present analysis could be a mixture of the contribution from the Galactic
center and the ridge. The diffuse component obtained here is the average over 12
degrees along the scan path and we assume two point sources within 1 degree from
the Galactic center. In fact, only one of them (No.5 in the scan No.2) shows a very
strong line emission. Therefore a large part of the iron line emission region near the
Galactic center would be included in the spectrum of the point source No.5. The
concentration of the iron line emission near the Galactic center suggests that the
continuum flux from this region (within 1 ° from the Galactic center) is about 10 %
of the whole ridge intensity.

In the scan No.6, the iron line is significantly broad and the center energy turns out
to be lower and not consistent with 6.7 keV. This kind of distortion can be explained
if the slope of the spatial distribution of the diffuse emission varies with the energy,
i.e.the apparent temperature of the ridge emission differs from place to place. This
possibility will be examined later in the spatial distribution section.

Next, we fit the energy spectra by absorbed Raymond-Smith models. The fit
becomes worse, and none of the 5 spectra show acceptable fits at 90% confidence
level (table 5.5). The data still exceed the model in the high energy band as shown
in figure 5.12. From these spectral fits by thermal emission models, we conclude that
the energy spectrum of the ridge component can not be explained by the simple hot
plasma emission alone.

The disagreement between the thermal model and the observed spectra is demon-
strated in the left panel of figure 5.12. There is an excess in X-ray emission over
the model above 10 keV, as if the spectrum has a hard tail. Based on this consid-
eration, we fit data with an absorbed power-law + Gaussian line model even though
the model does not naturally explain the iron line emission. This model turns out to

scan path	absorption	Fe-line		Thin thermal	χ^2/d.o.f
No	$N_H(10^{22}cm^{-2})$	center E(keV)	EW (eV)	kT(keV)	
1	<1.0	6.70 ± 0.20	643 ± 118	8.19 ± 1.02	18.5/12
2	<0.8	6.72 ± 0.04	1060 ± 80	7.65 ± 0.70	22.8/12
3	<5.9	6.72 ± 0.22	544 ± 230	6.25 ± 1.15	14.0/12
5	<3.4	6.68 ± 0.22	623 ± 210	10.3 ± 1.90	9.7/12
6	<2.1	6.60 ± 0.08	906 ± 120	7.81 ± 0.47	10.6/12

Table 5.4: Parameters of energy spectra (4.0-13.8keV) fitting by absorbed (thermal bremsstrahlung+Gaussian) models

scan path	absorption	Raymond-Smith		χ^2/d.o.f
No	$N_H(10^{22}cm^{-2})$	kT(keV)	abundance	
1	0.0	5.2	0.44	84.7/16
2	0.0	5.4	0.84	67.9/16
3	0.0	5.3	0.33	19.4/16
5	0.23	8.0	0.45	28.2/16
6	1.6	6.4	0.55	48.8/16

Table 5.5: Best fit parameters of energy spectra (2.3-13.8keV) fitting by absorbed Raymond-Smith models

give an acceptable fit to all the data (table 5.6). Therefore, it is likely that there is a power-law like hard X-ray component associated with the Galactic ridge emission.

Analysis of the averaged energy spectrum

To study the spectral feature of the overall ridge emission in more detail, we average five energy spectra (No.1-3,5,6) and fit it by several emission models including various thermal emission. The results are summarized in figure 5.13 and in table 5.7.

scan path	Fe-line		power law(4.0-13.8keV)	
No	center energy(keV)	equivalent width(eV)	photon index	χ^2/d.o.f
1	6.70 ± 0.09	795 ± 120	2.23 ± 0.10	8.81/12
2	6.71 ± 0.04	1260 ± 130	2.24 ± 0.08	13.6/12
3	6.71 ± 0.20	728 ± 250	2.45 ± 0.18	13.7/12
5	6.68 ± 0.21	769 ± 200	2.05 ± 0.12	8.8/12
6	6.59 ± 0.06	1270 ± 155	2.28 ± 0.06	9.7/12

Table 5.6: Parameters of energy spectra fitting by absorbed (power law +Gaussian) models
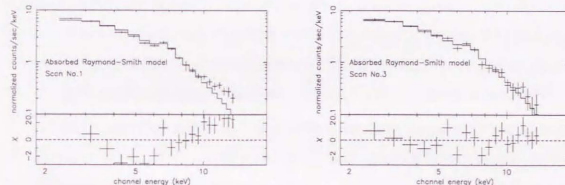
Figure 5.12: Fitting the energy spectrum of scan No.3 and Scan No.1

First we fit the spectrum with an absorbed thermal bremsstrahlung + Gaussian line model. As we have seen in the previous subsection, the hard tail in the spectrum is clearly present. The best fit value of the temperature becomes as high as 8.4 keV (figure 5.13 (a)). The center energy of the Gaussian line is 6.7 keV and the equivalent width is about 800 eV which corresponds to an iron abundance of about 0.8 solar abundance (figure 5.15) assuming that the solar ratio of the iron number relative to hydrogen is to 4×10^{-5} (Allen, 1976). Even with this high temperature, the data exceed the model function in the hard band and the fitting result is not statistically acceptable. As shown in figure 5.15, the iron line at 6.7 keV indicates that there is at least a thermal plasma with $kT < 6$ keV. Plasma with higher temperature should

show the line center energy significantly higher because of the enhancement of the 6.9 keV line. Using this simple model, the continuum and the iron line emission show different temperature. Furthermore, the continuum spectrum above 10 keV indicates that there is clearly a hotter ($kT > 10$ keV) or non-thermal component in addition to this thermal emission as shown in figure 5.11 (a).

To confirm that the ridge emission cannot be explained by the simple thermal emission models, we employ other thermal models. Raymond-Smith model (Shafer *et al.*, 1994) is known to reproduce emission include lines by a thermally equilibrium plasma. The purpose of using this model for the spectral fitting is to equalize the temperature of the continuum and the line emission with each other. We use the pulse -height spectrum between 3.0 keV and 18.0 keV because emission lines from sulphur, argon and other elements should appear in the low energy band. The best-fit temperature becomes as high as 6.7 keV, but there still remains an excess structure in the high energy band (figure 5.13 (c)). The thermal emission model from the hot plasma in thermal and ionization equilibrium state fails to explain the ridge emission.

We then use a non-equilibrium ionization model for SNRs by Masai (1984) to explain the co-existence of emission lines indicating different plasma temperature as reported by *Tenma* (Koyama *et al.*, 1986) and *Ginga* pointing observations (Yamauchi and Koyama, 1995). As shown in figure 5.13 (d), the value of ionization degree nt(s/cc) becomes as large as $10^{10.9}$ but the fit is not statistically acceptable. This results clearly indicates that the data are not compatible with thermal models even allowing for non-equilibrium plasma. Association of the hard component with the galactic ridge emission seems certain since essentially the same spectral feature is commonly observed in all the scan data along the Galactic plane.

If we go further with thermal emission models to explain the ridge emission, we should use multi temperature models or multi ionization degree models. If we had enough good energy resolution to determine the temperature and the ionization degree by emission lines, applying these models to the spectrum would be meaningful. However these models are too complicated to the quantity of the current energy spectrum. It is also apparent that neither of them could produce the "hard tail "

above 10 keV. So we give up to fit the energy spectrum only with thermal emission models and will look for the model function representing the spectrum.

We then fit the spectrum by an absorbed power law + Gaussian model . Though this model is not directly connected to a simple emission mechanism, the result turns out to be acceptable (figure 5.13 (b)). This suggests that there is a hard component in the ridge emission as well as a hot plasma component as indicated by the iron emission line at 6.7 keV.

Finally we employ an absorbed Raymond-Smith + absorbed power-law model (figure 5.14). The spectrum is represented by a slightly absorbed (N_H=(1.3±0.6) $\times 10^{22}$cm^{-2}) Raymond-Smith component with a temperature (3.1±1.4) keV and a strongly absorbed ($N_H \geq 4\times 10^{23}$cm^{-2}) power-law component with photon index (1.6±1.1) . We do not strictly take this model as the true emission mechanism of the ridge emission. This model is rather artificial and the difference of the hydrogen column density between the thermal and the power-law component is hard to be explained. This model represents only the characteristic shape of the energy spectrum such that the thermal component is accompanied by a strong "hard tail".

5.1.5 Spatial distribution

In this section we examine the spatial distribution of the ridge emission based on the intensity profile obtained by the scan fitting as summarized in table 5.8.

To approximate the spatial distribution of the diffuse emission intensity, we assume a thin finite disk which is uniform in radial direction and decreases exponentially in perpendicular to the Galactic disk ;

$$I = I_0 \times \exp\left(-b/b_0\right) \times \sqrt{1 - (\sin l/r_0)^2} \tag{5.1}$$

where b_0 denotes the projected scale height of the exponential disk, r is the radius of the emission disk, R is the distance between the Earth and the Galactic Center and r_0 is defined as r/R. As illustrated in figure 5.16, the depth of the disk in the line of sight is proportional to $\sqrt{r_0^2 - \sin^2 l}$.

Parameters of bremsstrahlung +Gaussian fit

absorption	N_H 10^{22}	0.0
bremsstrahlung	temperature(kT)	8.43
	normalization*	22.5
Gaussian	center energy	6.66
	sigma	0.0
	equivalent width	706
χ^2/d.o.f	40.36/12=3.363	

* normalization K = exp(1/kT(keV)) /Gaunt factor(kT)

Parameters of power-law + Gaussian model

absorption	N_H 10^{22}	1.95±2.4
power law	photon index	2.33±0.13
	normalization* 165±57	
Gaussian	center energy	6.68±0.05
	sigma	<0.24
	equivalent width	822±65
χ^2/d.o.f	17.19/12=1.432	

* normalization K = photons /keV/s/4000cm^2 at 1keV.

Parameters of Raymond-Smith model

absorption	N_H 10^{22}	0.0
Raymond	temperature(kT)	6.70
	abundance*	0.50
	normalization**	222
χ^2/d.o.f	111.6/17=6.56	

* 1 solar abundance = 4.68×10^{-5} iron atoms relative to hydrogen
** normalization K = $10^{-14}/(4\pi\ D^2 \int n^2\ dV)$

Parameters of Masai model

absorption	N_H 10^{22}	1.23
Masai	temperature(kT)	7.31
	abundance	0.62
	log(nt/(s/cc))	10.9
	normalization*	19528
χ^2/d.o.f	72.3/16=4.52	

* normalization K = $10^{-12}/(n^2\ V)$

Parameters of Raymond-Smith +power-law model

absorption	N_H 10^{22}	1.30 (-64 +2.0)
Raymond	temperature(kT)	3.10±1.4
	abundance	0.67(-0.17 +4.3)
	normalization	351(-70 +130)
absorption	N_H 10^{22}	37.8 (-0.1 +66)
power law	photon index	1.58 (±1.05)
	normalization	24.1 (-0.1 +395)
χ^2/d.o.f	19.87/15=1.42	

Table 5.7: Parameters of fitting results for various models

(a)   (b)

(c)   (d)
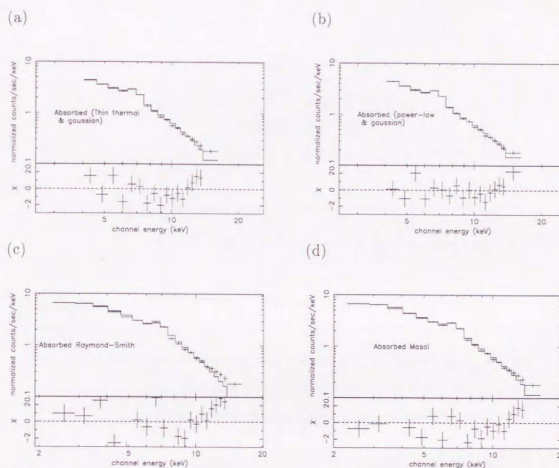
Figure 5.13: Fitting results of averaged energy spectrum, top left:absorbed thermal bremsstrahlung,top right:absorbed power-law,bottom left:absorbed Raymond-Smith,bottom right:absorbed Masai model

With this model, we fit the intensity profile of the scan data No.1−6 whose intensities are summarized in table 5.8. The parameters I_0, b_0 and r_0 have been varied to minimize the total χ^2 for each of the for energy bands. The result of the fit is summarized in table 5.9. Here the unit of I_0 is counts $\sec^{-1}$ $\mathrm{str}^{-1} LAC^{-1}$ at $(l, b) = (0, 0)$.

A reasonable fit is obtained for the spatial model described here for all energy bands. Obtained parameters are summarized in table 5.9.

The goodness of the fit is checked by comparison between these parameters and slope parameter $B(E)$ used in the scan fitting No.6 (20.5< l <37.5, see figure 5.6 and
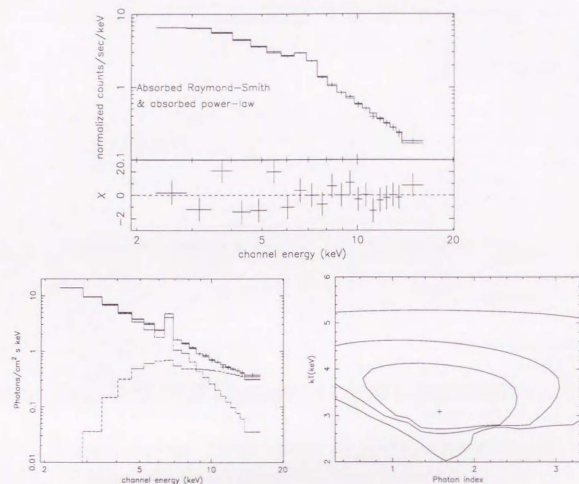
Figure 5.14: Fitting results of averaged energy spectrum by Raymond-
smith + power-law model

5.17) where the diffuse component significantly varies with the Galactic longitude.
Using the equation 5.1, the slope at $l = l_0$ is described as follows;

$$B'(l_0) = \frac{\partial I/\partial l(l_0, b)}{I(l_0, b)} = -\frac{\pi}{180} \times \frac{\sin l_0 \cos l_0}{r_0^2 - \sin^2 l_0} \tag{5.2}$$

The calculated value $B'(l_0)$ by the equation 5.1 and the slope parameter $B(E)$ from
the scan No.6 is summarized in table 5.10. Though these values are obtained inde-
pendently, they agree well except for the low energy band. This agreement shows
propriety of using simple finite disk model to describe the intensity profile of the
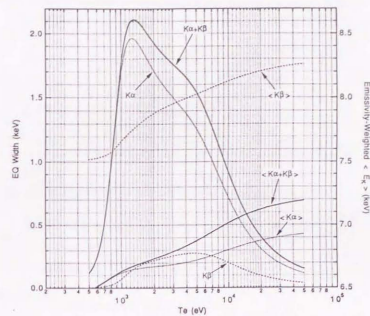
Figure 5.15: Iron K line equivalent width and center energy as a func-
tion of temperature, the abundance is fixed to one solar
(Allen, 1976). (Masai, private communication)

scan path	counts/sec/LAC			
No.	2.30~16.1keV	1.15~3.45keV	3.45~6.33keV	6.33~16.1keV
1	23.4±0.2	10.9±0.1	9.6±0.3	6.1±0.1
2	29.4±0.3	12.5±0.2	12.4±0.2	8.2±0.2
3	27.2±0.5	10.7±0.3	10.3±0.3	6.2±0.3
4	1.9±0.5	1.5±0.2	0.9±0.3	0.1±0.4
5	34.8±0.6	11.3±0.2	14.4±0.4	10.4±0.3
6	23.8±0.2	7.0±0.1	10.4±0.1	6.9±0.1

Table 5.8: Count rates of the diffuse component
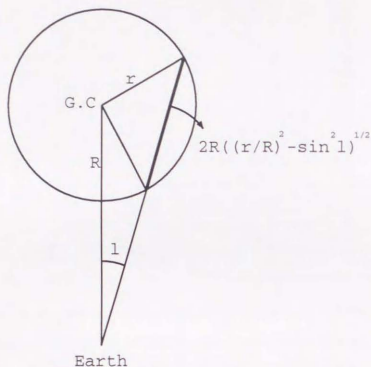
Figure 5.16: Illustration of the uniform disk model, $r_0 = r/R$

Energy band	I_0	$b_0(degree)$	r_0	χ^2/d.o.f.
2.3~16.1keV	$(7.2\pm1.1)\times10^4$	3.0 ± 0.7	0.72 ± 0.19	1.60/3
1.15~3.45keV	$(2.7\pm0.3)\times10^4$	4.1 ± 0.8	0.57 ± 0.05	2.70/3
3.45~6.33keV	$(3.0\pm0.5)\times10^4$	3.2 ± 0.8	0.73 ± 0.20	0.20/3
6.33~16.1keV	$(2.3\pm0.5)\times10^4$	2.3 ± 0.9	0.68 ± 0.16	0.48/3

Table 5.9: parameters of the exponential thin disk, I_0 is in unit of
counts sec^{-1} $\text{str}^{-1}LAC^{-1}$ at $(l,b) = (0,0)$

Energy(keV)	Scan fitting No.6	Table 5.9
	B (%/degree)	B (%/degree)
1.15~3.45	-4.8 ± 0.5	$-9.5^{+4.1}_{-6.7}$
3.45~6.33	-4.4 ± 0.4	$-2.7^{+1.5}_{-10.2}$
6.33~16.11	-5.8 ± 0.5	$-3.5^{+1.8}_{-18.6}$

Table 5.10: $A(E)$ and $B(E)$ obtained by scan fitting of No.6 and the
slope calculated by the parameters in table 5.9

ridge emission. In the low energy band, the systematic errors in the CXB subtraction would still be significant.

The spatial distribution of the ridge emission above 4 keV is therefore well described by the uniform disk model with a radius of about 5 kpc, and a scale height of 400 pc assuming that the distance between the earth and the Galactic center R is 8 kpc (Reid, 1993). The obtained scale height $\sim$ 400 pc is between that of the disk component 100 pc at $|l| >10°$ and that of the bulge component obtained by 6.7 keV line mapping (Yamauchi and Koyama, 1993). As our scan paths include the buldge region, the scale height is probably influenced by both. The emitting volume is estimated as follows with a scale height h_0 and a filling factor η which is a volume ratio of the emitting region in the interstellar space.

$$\begin{aligned} V &= \pi r^2 \times 2h_0 \times \eta \\ &= 2\pi R^3 r_0^2 \tan b_0 \times \eta \\ &= (2.6 \pm 0.9) \times 10^{66}\eta \; (\text{cm}^3) \end{aligned} \qquad (5.3)$$

5.1.6   Luminosity of the ridge emission

In this section, we calculate the luminosity and some parameters of the Galactic ridge emission using the energy spectrum and the spatial distribution obtained in the previous section.
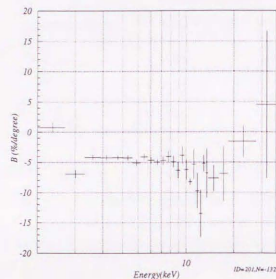
Figure 5.17: The slope B(E) vs energy at l=30° obtained in scan fitting No.6

The total intensity between 2.3 keV and 16.1keV at $(l,b) = (0,0)$ becomes $(7.2\pm1.1)\times10^4$ counts sec^{-1} str^{-1} for the LAC area as shown in the table 5.9. Assuming that the energy spectrum is described by a power-law with a photon index 2.2, the flux is

$$F = (2.1 \pm 0.3) \times 10^{-7} \text{ (erg cm}^{-2} \text{ sec}^{-1} \text{ str}^{-1}). \tag{5.4}$$

Since F corresponds to the surface brightness at the galactic center, the volume emissivity ε is given by the following relation ;

$$\frac{F}{R^2} = \frac{\eta\varepsilon}{4\pi R^2} \times 2r, \tag{5.5}$$

where $\eta < 1$ is a filling factor. This leads to

$$\varepsilon = (7.2 \pm 1.5) \times 10^{-29}\eta^{-1} \text{ (erg cm}^{-3} \text{ sec}^{-1}) \tag{5.6}$$

Using the emitting volume, the total luminosity of the ridge between 2.3 and 16.1 keV is estimated $(1.9\pm0.8)\times10^{38}$ erg sec^{-1}.

If we assume that all of the ridge emission is produced by a process of thermal bremsstrahlung, we can use the formula of the volume emissivity (Rybicki and Light-man, 1979).

$$\frac{dP(T)}{dV\,d\nu} = 6.8 \times 10^{-38} Z^2 n_e n_Z T^{-1/2} \exp(-E/kT) \bar{g_{ff}} \text{ (erg cm}^{-3} \text{ sec}^{-1} \text{ Hz}^{-1}) \tag{5.7}$$

$$= 2.4 \times 10^{-15} Z^2 n_e n_Z (\frac{kT}{keV})^{-1/2} \exp(-E/kT) \bar{g_{ff}} \text{ (keV cm}^{-3} \text{ sec}^{-1} \text{ keV}^{-1}) \tag{5.8}$$

where $\bar{g_{ff}}$: the velocity averaged Gaunt factor approximately represented as $(E/kT)^{-0.4}$

T : the electron temperature,

Z : the atomic number of ions, and

n_e and n_Z : electron and ion number densities respectively.

Assuming that the plasma has cosmic abundances and the electron temperature of about 8keV (see table 5.7), we obtain the electron density n_e by comparing equations 5.8 and 5.6.

$$\langle n_e^2 \rangle = (6.5 \pm 1.3) \times 10^{-6}\eta^{-1} \text{ (cm}^{-6}) \tag{5.9}$$

$$\langle n_e \rangle = (2.5 \pm 0.3) \times 10^{-3}\eta^{-1/2} \text{ (cm}^{-3}) \tag{5.10}$$

We note that the volume emissivity and the electron density are dependent on the filling factor η, this effect has been neglected in previous works (Koyama et al., 1986; Koyama et al., 1986). From the several spectral fittings shown in the previous section, the abundance of the iron is larger than 0.5 solar. This implies that the total mass of iron responsible for the line emission in the ridge is $(4\sim10)\times10^3 M_\odot$. At least 10^4 supernovae explosions are necessary to produce this amount of iron, even all the supernovae were type I.

5.2   Results from Welcome-1

5.2.1   Count rate history during the observation

As explained in section 4.2, *Welcome−1* telescope observed the Galactic center region (GC scan) and the Galactic plane including a well-known black hole candidate GX339-4 (Galactic plane region) on December 3 1991. The observed sky area are shown in figure 4.11 and 4.12.

The azimuthal angle of the telescope during the observation of the Galactic plane region is shown in figure 5.18. The elevation angle of the telescope was fixed at 68.9°, close enough to observe GX339-4 whose elevation was between 62.5° and 63.7°. The count rate history is shown in figure 5.19 where the difference between on-source and off-source observations appears clearly even though it took about one minute to stabilize the attitude of the detector after the rotation. The distributions of these count rates during the on-source and off-source observations after the event selection are shown in figure 5.20, and they are consistent with Poisson distribution. The average count rates for on-source and off-source observations are significantly different, confirming the detection of the emission from the on-source region.

After the gain correction and the event selection as described in chapter 4, we obtained the pulse height spectra for the on-source and off-source observations. For the GC scan, we subtracted the pulse height spectrum of the off plane scan from the data. For the Galactic plane observation, we added the pulse height spectra of four on-source and four off-source observations separately. Then the spectrum of the off-source observation was subtracted from the combined spectrum.

5.2.2   Obtained energy spectra of the Galactic center region

We obtained the energy spectrum from the Galactic center region as shown in figure 5.21. The result has been corrected for the detection efficiency, and for for the angular response.

As the field of view of *Welcome−1* is as wide as 16° in FWHM, these obtained flux could contain both the diffuse emission and the point source emission. In the Galactic center region there are many point sources in the hard X/γ ray band, and most of which are known to be time variable. So it is very difficult to estimate individual point source contribution in this *Welcome−1* observation. However we can simply set an upper limit for the diffuse ridge emission, assuming that the whole flux is due to the diffuse emission.

Then we fit the pulse height spectrum by a single power-law model, and the resultant parameters are summarized in table 5.11. Convolving the spatial distribution of
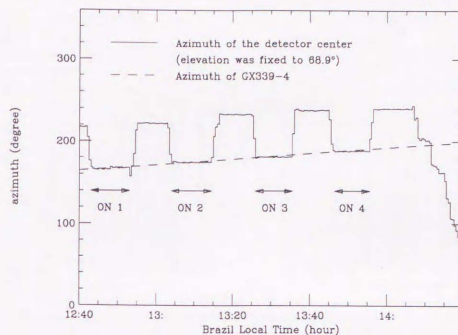
Figure 5.18: Azimuth of the detector and GX339-4
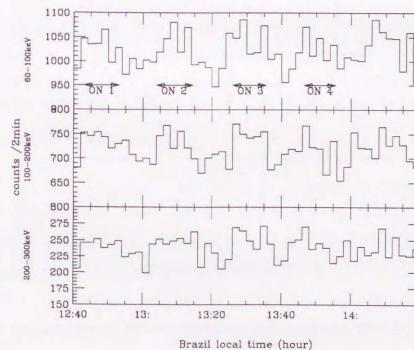
Figure 5.19: The count rates obtained during the galactic plane observation
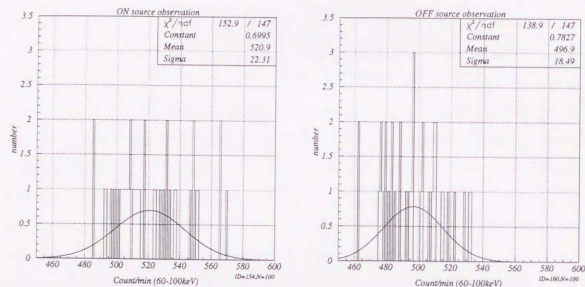
Figure 5.20: The distribution of the count rate between 60keV and 100keV, left panel:on-source observation right panel:off-source observation; The best fit Gaussian curve is shown in each figure.

the Galactic ridge emission obtained by the LAC in the previous section 5.1.5 through the angular response of $Welcome-1$, the effective solid angle of this observation is $(1.5\pm0.1)\times10^{-2}$ steradian after the on-off subtraction.

GC scan :1991 Dec.3 FOV=$\pm8°$		
Fitting range (keV)	40–300	
Photon index α	2.96	±0.17
Intensity at 100 keV (ph/cm^2/sec/keV)	7.86×10^{-5}	$\pm5.5\times10^{-6}$
χ^2	12.59	d.o.f =7

Table 5.11: The parameters of the single power-law fitting for the energy spectrum of the GC scan
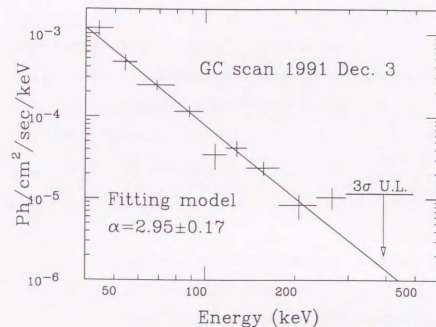
Figure 5.21: Flux from the GC region with no correction for the angular response

5.2.3 The energy spectrum of the Galactic plane and the diffuse component

The energy spectrum obtained from the Galactic plane region is shown in figure 5.22. It is not corrected for the angular response of $Welcome-1$. In the Galactic plane region, GX339−4 is almost the only hard X-ray source From the separation angle between GX339−4 and the filed of view center of $Welcome-1$, the time averaged detection efficiency for GX339−4 is 0.62± 0.05. GX339−4 is monitored continuously by $BATSE$ on board the CGRO satellite. On the day Dec 3 1991, the intensity of GX339−4 is below the sensitivity of BATSE which is about 100 mCrab (Harmon et al., 1993). The flux history monitored by $BATSE$ is shown in figure 5.23. SIGMA observed GX339−4 on 1991 October 5 and its intensities are 80±17 mCrab between

40 keV and 77 keV and 40±19 mCrab between 77 keV and 160 keV (Bouchet, 1992).
OSSE also observed GX339−4 on 1991 November 7∼12 and the best fit value for
the flux at 100keV is $(3.9\pm0.5)\times10^{-6}$ photons cm^{-2}sec^{-1}keV^{-1} or (Grabelsky et al.,
1995). The obtained spectrum between 70 keV and 120 keV is shown in figure 5.24
and in figure 5.22. However, the time variation of th eintensity of GX339−4 in low
state has not been observed nor stuided. It is considered to be independent from that
in X-ray band (Grabelsky et al., 1995). So we do not have the further information
about the intensity of GX339−4 on that day.
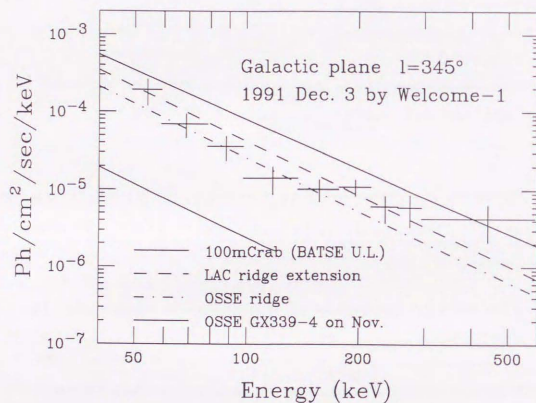
Figure 5.22: Flux from the Galactic plane including GX339−4, not
corrected for the angular response.The upper limit of the
flux of GX339−4 obtained by BATSE and the flux level
on Novermber 7∼12 by OSSE is

In figure 5.22, we also indicate the level for a source of 100 mCrab with a photon
index 2.1, which is an upper limit obtained by *BATSE* on that day, by the upper solid
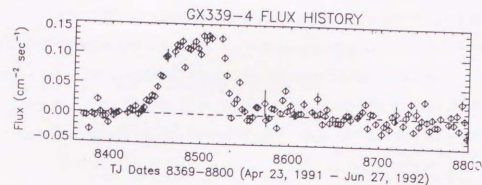
Figure 5.23: The intensity of GX339−4 in the 20-320keV band moni-
tored by BATSE. Each point represents a three-day aver-
age of the flux (Harmon et al., 1993). The day December
3, 1991 corresponds to 8594 in TJD
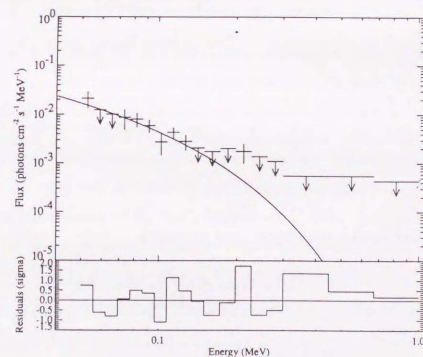
Figure 5.24: Energy spectrum of GX339−4 for the 1991 November
OSSE observation

line. The flux observed by *Welcome−1* is consistent with the *BATSE* observation. If the intensity of GX339−4 is same as that of OSSE observation on November, the contribution of GX339−4 is about 10 % of the observed flux.

The middle dashed line shows an extension of the Galactic ridge emission obtained by *LAC* in the previous section 5.1.4 with the spectral parameters shown in table 5.7. The effective solid angle of *Welcome−1* is calculated as $(2.1\pm0.1)\times10^{-2}$ steradian by convolving the spatial distribution of the ridge emission and the angular response of the detector.

The lower dot-dashed line shows a diffuse emission obtained by *OSSE* at $l = 25°$ (Purcell *et al.*, 1995) considering that the field of view of *OSSE* is 1.3×10^{-2} steradian or 0.62 times that of *Welcome−1* . The ridge emission obtained by *OSSE* is consistent with the extension of *LAC* within a factor of 2. The observed flux by *Welcome−1* is, if the flux of GX339-4 is less than about 20 mCrab, also consistent with both results. This flux is also considered to be an measured value for the Galactic ridge emission between 40 keV to 600keV which would include about 10 % contamination from GX339-4.

If the Galactic ridge emission is weaker than that of GX339-4, it is the first detection of the emission up to 600 keV from GX339-4 in low state. After correcting the angular response assuming that all of the observed flux comes from GX339-4, we fit the energy spectrum by a single power law model. The resultant parameters are summarized in table 5.12.

5.3   Combined energy spectrum

Figure 5.25 shows the wide band spectrum of the Galactic ridge emission obtained by *LAC* and *Welcome−1* and other instruments. The surface brightness obtained by *LAC* is translated to the flux from the central radian of the Galactic plane. The relation between the surface brightness and the flux from the central radian is shown by equation 2.2. In the central radian, the surface brightness can be approximated as

$$I(l, b) = I(0, 0) \times \exp(-|b|/b_0) \tag{5.11}$$

when the surface brightness is constant along the galactic plane in the central radian. Note that this gives an under estimation because the Galactic center emission is neglected. Then substituting equation 5.11 in equation 2.2, the flux from the central radian is represented as

$$
\begin{aligned}
F_{rad} &= \int_{-1/2}^{1/2} dl \int_{-\pi/2}^{\pi/2} \cos b\, db\, I(l, b) \\
&= 2 \int_{0}^{\pi/2} \cos b\, db\, I(0, 0) \times \exp(-b/b_0) \\
&\sim 2(\frac{b_0}{rad}) I(0, 0)
\end{aligned}
\tag{5.12}
$$

when $b_0 \ll \pi/2$.

Welcome−1 observed only a small part of the Galactic plane. So we estimate the upper limit in the following way. The flux observed by *Welcome−1* is translated to the surface brightness at the Galactic center assuming that the spatial distribution in this energy band is same as that obtained by the *LAC* . This gives the flux from the central radian using equation 5.12. The observation of the Galactic plane results in a lower upper limit for the Galactic ridge emission than the GC scan data. The difference should be due to contamination from point sources in the Galactic center region .

As we studied in the previous section 5.1.4, the energy spectrum obtained by the *LAC* shows a single power-law shape around 10keV and above, although the strong iron K-line indicates that the emission below 10 keV originates in a hot plasma. Figure 5.25 suggests that this power law shape emission in the X-ray band extends smoothly to the γ ray region (Yamasaki *et al.*, 1994; Yamasaki *et al.*, 1995). The dot-dashes line in the figure 5.25 shows a single power-law spectrum with a photon index 2.1 between 1 keV 10 100 MeV. It is interesting that if we assume a single power-law spectrum with index 2.1 ± 0.1 which connect the flux from *LAC* and *Comptel*, the limits given from the *Welcome−1* observation come very close to the assumed power-law model.
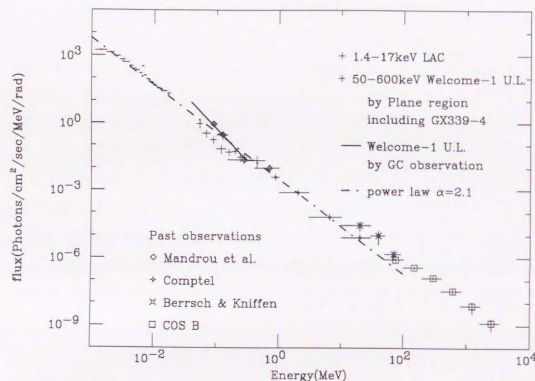
Figure 5.25: The wide band energy spectrum of the Galactic ridge emission, the intensity is normalized to that from the central radian. The observation by *Welcome-1* only sets an upper limit.

Chapter 6

Discussion

6.1 Summary of our observational results

The results on the diffuse hard X-ray emission from the Galactic ridge obtained in the present analysis are summarized in table 6.1. The X-ray emission is widely spread along the Galactic plane with a small scale height($\leq$400 pc) in agreement with previous measurement in the X-ray band (Yamauchi and Koyama, 1993). The energy spectra obtained from five scans at different regions resemble with each other. This resemblance, which is suggested by previous X-ray observations at selected source-free region, is measured directly by our observation and scan fitting analysis. The spectra show strong K-line emission from He-like iron with equivalent width of 500$\sim$ 1000 eV as has been observed by *Tenma* (Koyama *et al.*, 1986) and *Ginga* (Yamauchi and Koyama, 1993). The continuum emission is characterized by power-law like spectra with photon indices of 2.0$\sim$ 2.4 and inconsistent with a single-temperature thermal bremsstrahlung model implying that there is non-thermal component in the X-ray Galactic ridge emission. The existence of non-thermal component is shown directly for the first time by the high resolution energy spectra obtained above 10 keV in this observation. The total luminosity between 2 keV and 16 keV is as large as 10^{38} erg sec^{-1} in agreement with the past observations below 10 keV, and it is notable that about 25 % of the flux is radiated above 10 keV.

The observed flux from the Galactic plane at $l \sim 345°$ by *Welcome-1* is considered

Parameters	Values	Notes
Temperature(kT)	7.4 keV	Raymond-Smith model
	8.4 keV	Thin thermal bremsstrahlung
	3.1 ± 1.4 keV	Power law + Raymond-Smith
Surface brightness	$(2.1\pm0.3)\times10^{-7}$ erg cm^{-2}sec^{-1}str^{-1}	$2.3\sim16.1$keV
Spatial extent radius	(5.8 ± 0.9) kpc	for a uniform disk (R_{GC}=8kpc)
Scale height	$(4.1\pm0.6)\times10^2$ pc	for exponential distribution
Total volume	$(2.6\pm0.9)\times10^{66}\eta$ cm^3	η denotes a filling factor
Volume emissivity	$(7.2\pm1.5)\times10^{-29}\eta^{-1}$ erg cm^{-3} sec^{-1}	
Total luminosity	$(1.9\pm0.8)\times10^{38}$ erg sec^{-1}	
$\sqrt{<n_e^2>}$	$(2.5\pm0.3)\times10^{-3}\eta^{-1/2}$ cm^{-3}	solar abundance with kT =8.4keV
total iron mass	several$\times10^3 M_\odot\eta^{1/2}$	

Table 6.1: Characteristics of the observed ridge emission

to be dominated by the Galactic ridge emission. The result sets a tight upper limit for the ridge emission between 50 keV and 600 keV where few past observations exist. The flux is very close to a single power-law spectrum which connects the flux obtained by *LAC* and *Comptel*. This strongly suggests that there is a continuous emission from the Galactic ridge in the wide energy range between keV and 100 MeV. This is a completely new information on the nature of the Galactic ridge emission.

So the origin of the ridge emission is not a simple hot plasma under a thermal and ionization equilibrium state. These features are very unusual and cannot be interpreted in terms of a single species of known X-ray sources.

Based on the above results, we will discuss the nature and origin of the Galactic ridge emission. First, we shall reexamine whether the ridge emission is really diffuse or, instead, a sum of faint discrete sources. As shown later, known classes of X-ray sources can contribute only 20 % of the observed emission. Then we will discuss about the origin of the thermal component and the power-law component separately. SNRs

are shown to be the likely candidate of the thermal emission. The spectral index of power-law component suggests that electron bremsstrahlung is the underlying process. These consideration lead us to the interpretation that freshly accelerated electrons are continuously supplied in SNRs. Finally, we will investigate the possibility that a single acceleration process can produce both hot plasma and high energy electrons responsible for the "hard tail" and cosmic rays.

6.2   Possible unresolved point source contributions

The first step in our attempt of finding the origin of the Galactic ridge emission is to know whether it is really diffuse or a sum of faint point sources. For the non-thermal component, number of known Galactic X-ray sources whose spectra shows power-law shape above 10 keV is very small. According to the *Heao A-1* X-ray catalogue (Wood *et al.*, 1984), number of black hole candidates is 5 in total 842 X-ray sources above 0.3mCrab. Because of the lack of numerous point-source candidates, origin of the non-thermal component of the ridge emission is considered to be diffuse.

For the thermal component below 10 keV, there are many point sources which show thermal spectrum. We will estimate the contribution of the faint point sources to the thermal Galactic ridge emission in two different ways. One approach is the estimation of the total flux from the number-flux($\log N - \log S$) relation below our detection limit, and the other is the search for the candidate class of sources which account for the energy spectrum of the ridge emission.

First, we will estimate the contribution of the faint sources below the detection limit of the *LAC* , based on the $\log N - \log S$ relation by the IPC on board *Einstein X-ray observatory* (Hertz and Grindlay, 1984). In the present analysis, sources with the flux greater than 0.3 mCrab are identified in the scan fit. A source of 0.3 mCrab located at the Galactic center has the luminosity of 8×10^{34} erg sec^{-1}. The $\log N - \log S$ relation obtained by the *IPC* has a slope of -1 which is consistent with a two-dimensional disk population. The number-density relation for non coronal sources is

given by

$$N(> f_x) = 2.2 \times 10^{-3} f_x^{-1} \ (\text{degree}^{-2}) \tag{6.1}$$

f_x denote the IPC count sec^{-1} which is about 1 mCrab. Assuming the disk population, this can be transformed to a surface brightness for a face-on orientation as

$$\rho z \langle L_x \rangle = 4.0 \times 10^{28} \ (\text{erg sec}^{-1} \ \text{pc}^{-2}) \tag{6.2}$$

where ρ is the space density of sources in pc^{-3}, z is their scale height in pc and $\langle L_x \rangle$ is the mean X-ray luminosity of the sources in erg sec^{-1} (equation 24 in Hertz and Grindly,1984).
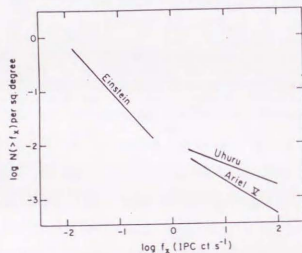

Figure 6.1: The $\log N - \log S$ relation obtained by the *IPC*, with 1 IPC count/sec corresponding to about 1 mCrab.(Hertz and Grindley, 1984)

Contribution from these discrete sources to the ridge emission can be obtained by coupling it with the observed spatial extent of the emission as follows;

$$\begin{aligned} \pi R^2 \rho z \langle L_x \rangle &= \pi \times 5800^2 \times 4.0 \times 10^{28} \\ &\sim 4 \times 10^{36} \ (\text{erg sec}^{-1}) \end{aligned} \tag{6.3}$$

The accounts for only 5% of the observed luminosity. Therefore, discrete X-ray sources observed with the *IPC* are unlikely to be the main origin of the X-ray ridge emission.

Some sources such as heavily absorbed objects, may still be a major contributor to the ridge emission. So we further search for the candidates in the known classes of

X-ray sources which can produce the Galactic ridge emission in the hard X-ray band. There are two requirements for the candidate; the luminosity of the individual source is less than 10^{35} erg sec^{-1} in order to escape from the point source detection in the scanning data, and the energy spectrum is as hard as that of the ridge emission. As the average X-ray luminosity of neutron star binaries is $10^{36\sim38}$ erg sec^{-1} (Hertz and Grindlay, 1984), typical low mass X-ray binaries and high mass X-ray binaries are excluded. For the stellar coronal sources, the temperature (typically below 1keV) is much lower than that of the ridge emission.

Once RS CVn type binaries have been considered as candidates to the ridge emission (Yamauchi, 1991). However, recent *ASCA* observation of RS CVns, for example AR Lac, show that the metal abundances of these class are a factor of 2 $\sim$4 below the solar value (White, 1994). Ottmann and Schmitt (1992) calculated the contribution of RS CVn to the iron line emission of the Galactic ridge emission to be 1 % at the maximum. From these consideration, RS CVns can be excluded from our list.

Cataclysmic variables (CVs) may make a contribution to the Galactic ridge emission. They can produce hard X-ray spectrum and strong iron line emission (Ishida, 1991). Yamauchi and Koyama (1993) excluded the possibility of CVs based on the difference between scale heights of the ridge emission and white dwarfs. However, a recent work by Patterson (1984) shows that the scale height of CVs distribution is 190±30 pc which roughly matches with that of the ridge emission. The luminosity and space density of CVs are summarized in table 6.2. The volume emissivity of the ridge emission is $\sim 10^{-28}$ erg sec^{-1} $\text{cm}^{-3} = 3 \times 10^{27}$ erg sec^{-1} pc^{-3}, and the most important CVs are the intermediate polars because of their high luminosities.

Fluctuation analysis of the surface brightness of the ridge emission in the recent *ASCA* observation indicates that at least 185 point sources are required in the FOV of *GIS* instrument (Kaneda *et al.* 1995, private communication) if all the ridge emission comes from discrete sources. The total volume of the Galactic ridge covered in the FOV (35′ diameter) is about 4×10^6 pc^3. The required space density of the point sources is several times 10^{-5} pc^{-3}. The space density of CVs as shown in table 6.2 is too low to account for the recent *ASCA* measurements. This is a new observational

evidence indicating CVs have little contribution to the Galactic ridge emission.

From these considerations, we conclude that the contribution of the point sources in the observed Galactic ridge emission is less than 20 %, which is the maximum fraction expected from CVs. The major part of the emission has to be diffuse in nature, unless entirely unknown class of objects contribute.

Class of CVs	luminosity (erg sec^{-1})	temperature (keV)	density (pc^{-3})
Dwarf Nova	10^{31}	10keV	$10^{-6\sim-7}$
Intermediate Polar	10^{33}	10keV	several $\times 10^{-7}$
Polar	10^{31}	10keV	a few $\times 10^{-7}$

Table 6.2: The luminosity, temperature, space density of CVs (Patterson, 1984 and Ishida, 1995 private communication)

6.3   Emission process of the diffuse ridge emission

In the previous section, we show that at least 80% of the observed ridge emission has a diffuse origin. Since the emission is extended over the Galactic plane and the observed energy spectra are similar from position to position, there is probably a common mechanism responsible for the ridge emission. The strong iron line emission suggests major contribution from a diffuse hot plasma ($kT \sim$ several keV) extended in the Galactic plane, even though it is not in an isothermal and ionization equilibrium state as indicated by the continuum emission spectrum. It seems unlikely that the emission from a hot plasma can account for a power-law like hard component which extends to MeV or GeV region. Therefore, we will first deal in the thermal component and then the non-thermal component separately.

6.3.1   Energy required to maintain the hot plasma

Here, we will look into the properties of the hot plasma required to explain the observed features. For the thermal component, we will estimate the necessary energy supply and condition required to maintain such a hot plasma. As we noted in the Chapter 5, taking the filling factor η into consideration is a important point. To estimate the necessary energy, we have to know the time scales for the radiation cooling and the escaping from the Galaxy.

Employing the observational results summarized in table 6.1, the kinetic energy of the plasma with a temperature of 8 keV in a unit volume is given by

$$2 \times \langle n_e \rangle \times \frac{3}{2}kT = (9.6 \pm 1.2) \times 10^{-11}\eta^{-1/2} \ (\text{erg cm}^{-3}), \tag{6.4}$$

where η denotes the filling factor. Dividing it by the volume emissivity for thermal bremsstrahlung, the cooling time is estimated as

$$\begin{aligned}\tau_{cool} &= \frac{3\langle n_e \rangle kT}{n_e^2 \Lambda(T)} \\ &= (4.1 \pm 1.0) \times 10^{10}\eta^{1/2} \ (\text{year}).\end{aligned} \tag{6.5}$$

As the hot plasma of thermal energy $kT = 8$ keV can not be confined gravitationally, the plasma should escape from the Galactic plane if there is no other confinement mechanism working (such as magnetic field). The sound velocity v_s of the hot plasma hydrogen with thermal energy $kT = 8$keV is 8.8×10^7cm sec^{-1} or 9×10^{-4} pc year^{-1}. Assuming that the escape velocity is given by $v_{esc} = v_s \times \delta$ ($\delta < 1$), the escape time τ_{esc} is given by the scale height z divided by v_{esc} as,

$$\begin{aligned}\tau_{esc} &= \frac{z}{v_{esc}} \\ &= (4 \pm 1) \times 10^5 \delta^{-1} \ (\text{year}).\end{aligned} \tag{6.6}$$

For $\delta > 10^{-5}$, the escape time is shorter than the cooling time. The main process for the energy loss is considered to be the gas escaping from the Galaxy without any confirmation mechanism.

The total energy of the hot plasma E_{total} is given by

$$E_{total} = 2 \times \frac{3}{2}kT\langle n_e \rangle V = (2.5 \pm 0.9) \times 10^{56}\eta^{1/2} \ (\text{erg}) \tag{6.7}$$

So the necessary energy supply is

$$\dot{E} = \frac{E_{total}}{\tau_{esc}} = \frac{(2.5 \pm 0.9) \times 10^{56} \eta^{1/2}}{(4 \pm 1) \times 10^{5} \delta^{-1}}$$
$$= (6 \pm 2) \times 10^{50} \eta^{1/2} \delta^{1} \text{ (erg year}^{-1}). \tag{6.8}$$

The most likely energy source to supply such a large amount of energy is considered to be supernovae (Koyama *et al.*, 1989) as described in Chapter 2. However, there are two unresolved problem that it requires high supernovae rate and that the heating process in SNRs is not clearly understood. We will check the potentiality of supernovae to supply the energy and the matter to the hot gas in consideration of the filling factor.

6.3.2 Supernovae as the energy source of the hot plasma

First, we will estimate the required supernova rate to supply the energy. If one supernova supplies an energy of $E_{SN} = \epsilon \times 10^{51}$ erg into the Galactic ridge plasma, the supernova rate should be

$$\frac{\dot{E}}{E_{SN}} = \frac{(6 \pm 2) \times 10^{50} \eta^{1/2} \delta^{1}}{\epsilon \times 10^{51}}$$
$$= (6 \pm 2) \times 10^{-1} \eta^{1/2} \delta \epsilon^{-1} \text{ (SNe year}^{-1}) \tag{6.9}$$

If the filling factor $\eta = 1 \times 10^{-3}$, a supernova should occur in every 50 year in the Galaxy. It is close to the previously estimated rate of once in every 20 years (Woosley and Weaver, 1986) as a crude estimation.

The number of supernovae needed to supply energy to the current ridge emission is

$$N_{Energy} = \frac{E_{total}}{E_{SN}} = (8.4 \pm 2.8) \times 10^{4} \eta^{1/2} \epsilon^{-1}. \tag{6.10}$$

The iron found in the Galactic ridge emission is several$\times 10^{3} M_{\odot} \eta^{1/2}$ (see table 6.1). If all of the iron comes from type I supernovae and each of them supplies iron of 0.8 $M_{\odot}$(Woosley and Weaver, 1986), the number of supernovae to provide the iron in the ridge is $N_{Fe} \leq 10^{4}$.

Since some fraction of iron may be kept in X-ray dark medium such as dust grains, N_{Fe} should be greater than N_{Energy},

$$(8.4 \pm 2.8) \times 10^{4} \eta^{1/2} \epsilon^{-1} \leq 10^{4}. \tag{6.11}$$

If filling factor $\eta^{1/2}$ is less than 0.1, both the total energy and iron in the Galactic ridge plasma can both be explained by supernovae. For example, if $\eta = 10^{-3}$ and $\epsilon \sim 1$, N_{Energy} becomes about 2500. It requires that the average age of SNRs is about $50 \times 2500 = 10^{5}$ year when SNRs is in so-called "snow-plow" phase. The typical radius R_{s} at that time is about 30pc (Longair, 1994b). Then the filling factor becomes $\frac{(4/3\pi R_{s}^{3}) \times 2500}{V_{total}} = 3 \times 10^{-3}$ which is almost consistent with the previous assumption.

To summarize, if the filling factor of the hot plasma η is less than $1 \times 10^{-(2 \sim 3)}$, the supernova rate and the number of supernovae necessary to account for the hot plasma turn out to be reasonable numbers as compared with the observations. The unresolved problem is the heating mechanism. The simple proposed mechanism is a shock heating in SNRs but the observed ridge temperature is higher than that of typical SNRs. The magnetic field in plasma may play an important role both in the confinement of the plasma and in the effective shock heating.

6.3.3 Emission process of the non-thermal component

Here we will look into the origin of the non-thermal Galactic ridge emission between 10 keV and 1 MeV. The combined energy spectrum shown in figure 5.25 approximated by a power-law model with photon index 2.1 ± 0.1 between 10 keV and 100 MeV. As shown in Chapter 2, possible processes of γ ray emission are bremsstrahlung and inverse Compton scattering below 100 MeV. The bremsstrahlung has been considered to be dominant in the energy range between 70 MeV and a few GeV.

Let us examine the spectral index if the hard X-ray spectrum for the inverse Compton process in which high energy electrons interact with low energy photons. The absolute flux is difficult to estimate because of the ambiguity of the density and temperature of infrared and starlight photons. However, the spectral index of the emission is defined by spectral slope of the high energy electrons above 100 MeV (see

Appendix A). Assuming that the index of electrons above 100 MeV is about $p = 2$ based on the observations described in Chapter 2, the expected index of the photon spectrum becomes $\alpha = (p+1)/2 = 1.5$, which is much flatter than the observed index of $\alpha = 2.1 \pm 0.1$. Therefore, it seems difficult to explain the hard X-ray ridge emission in terms of the inverse Compton process.

The difficulty of the inverse Compton model lead us to consider bremsstrahlung as the more promising process below 100 MeV. As show below, the bremsstrahlung can in fact account for the observed spectrum of the hard X-ray Galactic ridge emission.

If the hard X/γ-ray emission from the Galactic ridge is produced by electron bremsstrahlung, low energy electrons should have the spectrum with almost the same as the observed photon spectrum (see Appendix A) down to the energy of ~ 10 keV. In this case, the energy spectrum of cosmic electrons around 10 keV becomes very similar to that in the range between 100 MeV and 10 GeV namely a power-law form with the index ~ 2. This suggests that the spectral flattening below 100 MeV due to ionization loss in the interstellar space does not occur in the actual electron spectrum. As reviewed in Chapter 2, there has been no direct information about the cosmic electron spectrum in the interstellar space below ~ 100MeV mainly due to the solar modulation. The Galactic ridge emission in the hard X-ray band is, therefore, the only way to measure the spectrum of low energy electrons.

From these consideration, bremsstrahlung seems to be promising for the emission process of the Galactic ridge emission if enough amount of low energy (~ 10 keV) electrons are present in the emission region. The condition that the electron spectrum does not suffer a significant change from the $p \sim 2$ power-law form can be given by the thickness of matter electrons have penetrated. A simple calculation shows that the amount of matter which does not cause significant change in the electron spectrum at 10 keV due to ionization loss is about 15 μg cm^{-2}. If the ISM has a particle density of 1 cm^{-3}, the thickness corresponds to only 15pc. Therefore, we need to consider that the hard X-ray photons are created by the electrons before they travel significant distance in the interstellar space, or while electrons are still freshly accelerated. The close spatial association of the hard X-ray emission with the thermal soft X-rays

suggests that these two components may be produced in the same region. This gives an idea that the thermal electrons of the hot plasma work as injected electrons in an acceleration process to produce non-thermal electrons. The young SNRs would be a candidate where shock waves heat up the hot plasma and produce cosmic ray electrons.

6.4 Accelerated electrons in SNRs as the origin of the Galactic ridge emission

6.4.1 Co-existence of thermal and non-thermal electrons in SNRs

In the previous sections, we have discussed that the co-existence of the thermal and the non-thermal component in the Galactic ridge emission suggests that acceleration of thermal electrons in SNRs is the key mechanism to understand the overall features. The thermal component is produced by the thermal bremsstrahlung of the hot plasma heated in SNRs. The non-thermal "hard-tail" component is also produced via the bremsstrahlung of the non-thermal low energy electrons.

To produce the hard tail, we need electrons whose energy is higher than the thermal electrons in SNRs. On the other hand, if we would explain low energy γ ray flux in terms of the cosmic ray electrons, we need a large amount of newly accelerated low energy electrons. As the acceleration of the cosmic rays is considered to occur mainly in SNRs, our prime focus goes to the acceleration mechanism in SNRs.

In most of the previous models of the acceleration process, the flux and spectrum of the injected particles are a priori assumed and their origin is not questioned. Our question is, based on the assumption that the injected electrons are in the form of hot plasma in the shell of SNRs where a shock comes in, whether they can be efficiently accelerated up to the energy of 10keV $\sim$ GeV. If they can, then freshly accelerated electrons become promising candidates to explain the hard X-ray part of the Galactic ridge emission. This would give a consistent view of the whole energy spectrum from

the thermal component in keV band to the power-law component extending up to
GeV band.

The efficiency of the acceleration is determined by the balance of the energy gain
and loss of electrons (Hayakawa, 1969). The particle acceleration is achieved by re-
peating shock crossings in which a particle gains additional momentum in proportion
to its present momentum. During the shock crossings, particles also lose their en-
ergy by interactions with matter. If the particle lose more energy than the gain in
the last shock crossing, the acceleration does not occur effectively. Once electrons
acquire enough energy, they begin to be accelerated repeatedly to achieve very high
energy till they escape from the shock region. Since the density of the matter can
be estimated from the observed ridge emission, the energy loss rate can be easily
estimated. On the other hand, it is difficult to estimate the acceleration efficiency
because the time interval between the shock crossings and the energy gain during the
shock acceleration are very complicated and not well-modeled for the actual estima-
tion. Here, we will refer to the simple diffusive shock acceleration theory (Bell, 1978a;
Bell, 1978b) as a guide line and examine the possibility if the electrons in the hot
plasma can receive necessary acceleration for the cosmic rays.

6.4.2   Energy loss and gain in the acceleration process

The energy loss rate of low energy electrons in optically thin fully ionized gas is dom-
inated by the excitation of plasma oscillation, which is similar to the ionization loss
process (Hayakawa, 1969). The loss rate is, therefore, given by

$$(\frac{dE}{dt})_{ion} = 7.64 \times 10^{-9} \frac{n_e}{\beta}(\ln(\frac{\beta^2\gamma}{n_e}) + 74.8) \text{ (eV/sec)} \tag{6.12}$$

Here, n_e = electron number density in cm^{-3},

$\beta = v/c$,

γ = electron Lorentz factor .

We will estimate the acceleration rate using Bell's (1978b) treatment (see Ap-
pendix A). We simplify the equation C.1 assuming a strong shock condition $u_1 =$

u_s(shock velocity), $u_2 = u_1/4$ to obtain the most efficient acceleration. We also as-
sume a non-relativistic case, i.e. $T \sim \frac{1}{2}mv^2 \ll m_ec^2$. Then the acceleration rate is
given by

$$\Delta T/T \sim \frac{8(u_1 - u_2)}{3v} \tag{6.13}$$
$$\sim 2\frac{u_s}{v}$$

The estimation of the diffusion constant κ is a very difficult problem in the accel-
eration theory because the roll of magnetic field in the shock region is highly unclear.
Here we approximate it by using a mean free path of electrons l as

$$\kappa = \frac{lv}{3} \tag{6.14}$$

The value of l is estimated to be less than the thickness of the shell in SNRs in order
that the acceleration process works. Then the equation C.2 can be translated into

$$t_{cyc} \sim \frac{4}{v}(\frac{l_1v}{3u_1} + \frac{l_2v}{3u_2}) \tag{6.15}$$
$$\sim \frac{20l}{3u_s}.$$

The acceleration time is represented using the equation C.3 as

$$t_{acc} = \frac{20l}{3u_s} \times \frac{v}{2u_s} \tag{6.16}$$
$$= \frac{10lv}{3u_s^2}.$$

So the acceleration rate is roughly estimated as follows;

$$\frac{T}{t_{acc}} = \frac{3Tu_s^2}{10lv} \tag{6.17}$$
$$= \frac{3Tc\beta_s^2}{10l\beta}.$$

Apart from the $1/\beta$ dependence, the ionization loss rate is roughly in proportion
to the electron density n_e and the acceleration rate is in proportion to β_s^2/l (pc^{-1}),
which we hereafter refer to as "acceleration parameter" . The possible value of this
acceleration parameter in a shock region in SNRs is about 10^{-4} pc^{-1} for a typical value
of β_s =0.01 and l = 1pc. To make numerical comparison, we plot the equation 6.12
by taking n_e =$1\times10^{-3} \sim 1\times10^{-1}$ cm^{-3} ($\eta = 1\sim1\times10^{-4}$) and the equation 6.18 taking

the acceleration parameter $10^{-5} \sim 10^{-3}$ in figure 6.2. For electrons to experience an effective acceleration, the total energy balance should satisfy

$$\frac{dT}{dt} = \frac{T}{t_{acc}} - \left(\frac{dT}{dt}\right)_{ion} > 0. \tag{6.18}$$

The plot in figure 6.2 indicates that there are indeed possible combinations of parameters $n_e, \beta_s,$ and l which give positive value of dT/dt. From figure 6.2, the minimum kinetic energy T_{cr} of electrons to undergo an effective acceleration turn out to be on the order of 10keV. The electrons with energies below T_{cr} can be accelerated at the shock but lose more energy by the ionization loss. In other words, they are subject to a thermalization by the shock heating. The electrons with energy above T_{cr} can increase the energy during successive shock crossings. As the energy gain ΔT is proportional to T/v, the acceleration process works slowly at first. After electron energy becomes large enough (several $\times T_{cr}$), they do not lose energy by the ionization process and the acceleration process becomes ever more efficient.

From these consideration, the value of $T_{cr} \sim 10$ keV just satisfies our requirements. If T_{cr} were much higher than the electrons thermal energy, we would need to consider another process to accelerate charged particles in SNRs up to the comic rays. And if T_{cr} was the same or less than the thermal energy in the observed SNRs, the hot plasma in SNRs could not be thermalized. Our estimation shows that the thermal hot plasma in SNRs can work as the source of the injected electrons for the cosmic ray acceleration. The possible range for the critical kinetic energy T_{cr} would be between 2 keV and 200keV. The relation between electron density and the acceleration parameter to satisfy the condition for the positive acceleration is shown in figure 6.3.

6.4.3 Spectrum of the accelerated electrons in the hot plasma

Here we perform a brief simulation to see how the energy spectrum of electrons evolve with time. We assume that electrons are initially under a Maxwellian distribution of 3 keV and the density $n_e = 5 \times 10^{-3}$. As the shock condition, we employ the shock velocity $\beta_s = 0.01$ and the electron mean free path $l = 1$pc. Then, the typical cyclic time becomes 7×10^{10} seconds. The electrons with energy above $T_{cr} \sim 12$
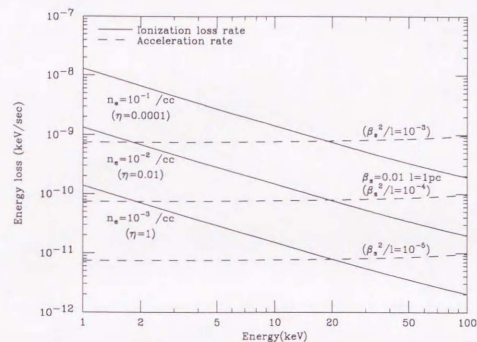
Figure 6.2: The energy loss and shock acceleration rate as a function of the electron kinetic energy. Three solid lines show the ionization loss rate of different electron densities, three dashed lines show the acceleration rate of different shock velocity.An crossing point of the solid and the dashed line gives a critical electron energy to start an effective acceleration.

keV are accelerated and lower energy ones loses their energy. Here, we neglect the thermalizing (hence, the energy loss) process because the typical ionization time scale is shorter than the electron-electron collision time scale. In figure 6.4, we plot the spectrum of the electrons in every 7×10^{10} sec. The resultant electron spectrum after the acceleration is presented as the sum of the spectra in each step. Here, we plot the spectrum for the sum of 10 steps ignoring the electron escape from the shock region in the left panel of figure 6.4. In the right panel of figure 6.4, the probability of escaping from the shock front in each step is assumed as $1/3$ independently of electron energy. These figures show a hard tail is produced from the thermal pool of
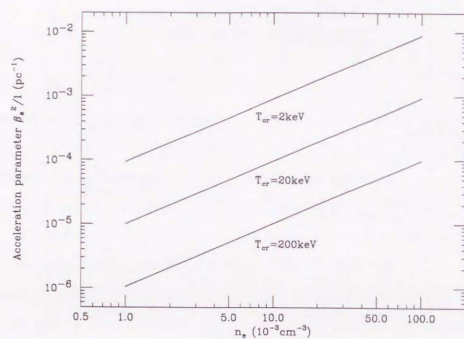
Figure 6.3: The acceleration parameter vs the electron density give
the critical electron energy of 2, 30 and 200 keV

the electrons by the diffusive shock acceleration. This simple simulation is successful
to produce a power-law tail in the thermal electron spectrum. The emission spectrum
from these electrons via bremsstrahlung would represent that of the observed ridge
emission, that is, almost thermal bremsstrahlung of several keV but with a hard tail
above 10 keV. At the same time, it shows a possibility that cosmic ray electrons can
be produced by the diffusive shock acceleration in SNRs from the thermal electrons.

In the actual situation, however, the geometry of the shock region should be
an important factor to determine the escape probability. The proper treatment of
shock geometry would be very complicated, and furthermore, the ridge emission is
considered to be the superposition of many SNRs. The simulation of the hard X-ray
spectrum carried out here is still crude, but the success of reproducing the hard tail
in the spectrum implies that the shock acceleration in SNRs is playing a major role
in producing both hard X/γ-ray emission from the Galactic ridge and cosmic ray
electrons.
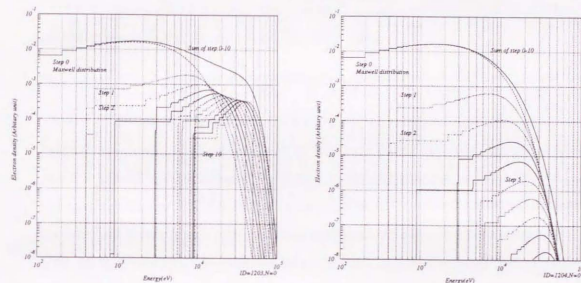
Figure 6.4: Energy spectra of the accelerated electrons from Maxwell
distribution of 3keV ($n_e = 5 \times 10^{-3}$cm^{-3}, $\beta_s = 0.01$,
$l = 1$pc, and $T_{cr} = 12$ keV). left:no consideration about the
escaping ,right:the escape probability of each step $= 1/3$

Chapter 7

Concluding remarks

In this thesis, we studied the Galactic ridge emission in the hard X–ray band. The results are summarized as follows;

1. The high-quality X-ray spectrum of the diffuse Galactic ridge emission is obtained between 3keV and 16 keV by scan fitting analysis which subtract the point source contribution in consideration of energy spectrum of each source. The energy spectrum of the Galactic ridge emission above 10 keV is obtained with good statistical accuracy for the first time. The resemblance of 5 energy spectra obtained in different scan regions suggests that there is a common physical process in the Galactic plane to produce hard X-ray emission.

2. The continuum spectrum of the Galactic ridge emission can not be fitted by a single temperature thin thermal bremsstrahlung model because of a "hard tail" above 10 keV. An acceptable fit is obtained with a power-law and a line model. The hot plasma in the Galactic ridge indicated by the existence of strong iron line emission is unlikely to be in thermal and a ionization equilibrium state. A mixture of an absorbed power-law and a thin thermal plasma models give a good fit to the data.

3. We have estimated possible contribution from the faint point sources below *Ginga*'s detection limit using the *Einstein* logN−logS relation for the Galactic

sources. We have also estimated the possibility of the CVs's contribution by the surface brightness fluctuation of the Galactic ridge emission obtained by *ASCA* and the space density of CVs. The point source contribution to the Galactic ridge emission in hard X-ray band is estimated to be 20 % at the maximum. The X-ray emission from the ridge is considerable to be diffuse in origin.

4. The observation of the Galactic plane at $l = 345°$ with a balloon born experiment *Welcome−1* set tight upper limits for the spectrum of the diffuse Galactic ridge emission. The limits lie on the smooth power-law connection of the hard X-ray data obtained by *LAC* and the γ ray data.

5. We have reexamined the possibility of supernovae to supply the energy and heavy elements for the diffuse Galactic ridge emission taking account of the proper treatment of the filling factor. We have found that the filling factor of $10^{-2 \sim -3}$ is suitable to explain the both supply with a supernova rate of one per several $\times 10$ year .

6. We have shown that the diffuse Galactic ridge emission in hard X-ray/ γ-ray band is considered to be produced by bremsstrahlung of low energy cosmic electrons. It suggests that the spectrum of the cosmic electrons extends down to several $\times 10$ keV with index ~ 2 in contrast to the expected spectral flattening at low energies due to ionization loss in the interstellar space. It requires that the electrons are still freshly accelerated.

7. A diffusive shock acceleration model is examined. In a thin hot plasma with a temperature of a few keV and an electron density $n_e \sim 10^{-2 \sim -3}$ cm^{-3}, electrons can be accelerated from a thermal velocity to non-thermal velocity under reasonable shock conditions in SNRs. In such a condition, a hot plasma would be accompanied with "hard tail" component. Although the model is still crude, the shock acceleration in SNRs is a promising picture in explaining the smooth extension of the Galactic ridge spectrum from keV to over 100 MeV region.

In this thesis, the relation between the hard X-ray and γ ray diffuse Galactic ridge emission has been pointed out for the first time. The co-existence of thermal and non-thermal electrons in SNRs is able to explain the spectral feature of the diffuse Galactic ridge emission. The hard X-ray emission is interpreted as a evidence of the shock acceleration to produce cosmic rays in SNRs. To establish this picture, the detailed study of the energy spectrum and the spatial distribution of the diffuse Galactic ridge emission between 10 keV and 1 MeV is required. It will be possible with *XTE* satellite and future *Astro-E* missions.

Appendix A

Emission from non-thermal electrons

Here, we summarize the emission from non-thermal electrons. The number spectrum of the electrons with a index p is shown by ;

$$N(E)dE = \frac{n_0}{E_0}(\frac{E}{E_0})^{-p}dE. \tag{A.1}$$

Hereafter, we use the notation of m_e as the electron mass, e as the unit charge, $\hbar$ as the Plank constant divided by 2π, c as the speed of light, α as the fine structure constant $e^2/\hbar c$, β as speed of a electron divided by c and γ as Lorenz factor of a electron.

A.1   Synchrotron radiation

In the magnetic field , accelerated charged particles emit synchrotron radiation. For single electron, the critical frequency is given by

$$\nu_c = \frac{3e}{4\pi}\frac{eH_\perp}{m_ec}\gamma^2\beta^2 \tag{A.2}$$

and the frequency where the emissivity is at maximum is given by

$$\nu_m = 0.29\nu_c \sim 1.22\gamma^2\frac{H_\perp}{\text{gauss}}\text{ MHz.} \tag{A.3}$$

117

where $H_\perp$ shows the strength of the magnetic field perpendicular to the electron motion. For example the peak frequency by the electrons with energy 5 GeV in the magnetic field of 3 μGauss becomes 360 MHz. The volume emissivity by the electrons with a power-law spectrum as shown in equation A.1 is shown as ;

$$
\begin{aligned}
J(\nu) &= n_0 y(p)\alpha h\nu_c(\frac{\nu}{\nu_0})^{-(p-1)/2} \\
&\propto n_0 H_\perp^{(p+1)/2}\nu^{-(p-1)/2}
\end{aligned}
\tag{A.4}
$$

where

$$
\nu_0 = \frac{3}{2}\nu_c(\frac{E_0}{m_e c^2})^2
$$

$$
y(p) = \frac{\sqrt{3}2^{(p-1)/2}\Gamma(\frac{3p-1}{12})\Gamma(\frac{3p+19}{12})\Gamma(\frac{p+5}{4})}{8\sqrt{\pi}(p+1)\Gamma(\frac{p+7}{4})}.
$$

Sample values of $y(p)$ are $p(1.5) = 0.147, p(2) = 0.103$ and $p(2.5) = 0.0852$. The spectral index of the emission is $(p-1)/2$.

A.2 Inverse Compton scattering

By the inverse Compton scattering with a electron of energy E and a photon with a energy ε, the average energy of the scattered photon is

$$
\bar{\varepsilon}' = \frac{4}{3}\varepsilon\gamma^2
\tag{A.5}
$$

The energy of the contributing electron to make the scattered photon with energy $\varepsilon' \pm \Delta\varepsilon'$ is shown by $\bar{\gamma} \pm \Delta\bar{\gamma}$ as

$$
\begin{aligned}
\bar{\gamma} &= \sqrt{\frac{3\varepsilon'}{4\varepsilon}} \propto \varepsilon'^{1/2} \\
\Delta\bar{\gamma} &= \frac{8}{3}\frac{\Delta\varepsilon'}{\varepsilon'}\frac{1}{\bar{\gamma}} \propto \bar{\gamma}^{-1}.
\end{aligned}
$$

In case of the ratio between the energy of photons and electrons is very large even if the distribution of the original photons are described by that of the black body radiation with temperature T and density n_{ph}, it is able to simplify the photon distribution by a delta function at average energy $\bar{\varepsilon} = 2.7kT$ with the number density

n_{ph}. Assuming that the energy of the scattered photon is 10 keV and the original energy kT of photons are 3K, 100K and 6000K, the required energy of the electron are 3GeV, 500 MeV and 60 MeV respectively.

When the distribution of the electrons follows a power-law as shown by equation A.1, the number of electrons contribution to make the scattered photon with energy $\varepsilon' \pm \Delta\varepsilon'$ is

$$
N(\bar{\gamma})\Delta\bar{\gamma} \propto \bar{\gamma}^{-(p+1)} \propto \varepsilon'^{-(p+1)/2}.
$$

Then the spectrum of the scattered photon is shown approximately by

$$
\begin{aligned}
p(\bar{\varepsilon}') &= \frac{1}{2}n_{ph}\sigma n_0(\frac{E_0}{m_e c^2})^{p-1}(\frac{3\varepsilon'}{4\bar{\varepsilon}})^{-(p-1)/2}\frac{1}{\varepsilon'} \\
&\propto n_{ph}n_0\varepsilon'^{-(p+1)/2},
\end{aligned}
\tag{A.6}
$$

where σ is Klein-Nishina cross section $\sim \sigma_{Th}$. Then the photon index of the scattered photon spectrum becomes $(p+1)/2$.

A.3 Bremsstrahlung

Calculation of cross section or emission spectrum by bremsstrahlung is not as simple as synchrotron radiation and inverse Compton scattering because the distribution of electrons in the target atoms is required. Accurate treatment of bremsstrahlung by relativistic and non-relativistic electrons down to 10 keV are summarized by Sacher and Schönfelder (1984) using the results of Koch and Motz (1959) and Blumenthal and Gould (1970). The cross section is shown in the figure A.1. A bremsstrahlung photon of energy ε is on average produced by an electron of kinetic energy 3ε. The photon index of the emission spectrum is almost as same as that of electrons with small discrepancy shown in figure A.2.
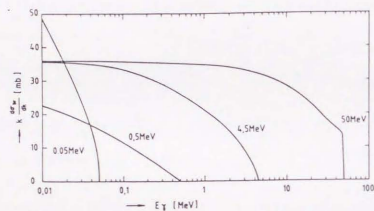
Figure A.1: Differential bremsstrahlung cross sections in atomic hydrogen for mono energetic kinetic electron energies (50 keV, 500 keV, 4.5 MeV, and 50 MeV) by Sacher and Schönfelder (1984)
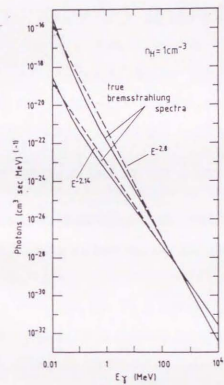
Figure A.2: Calculation of bremsstrahlung emission spectrum by artificial cosmic ray electrons of a single power-law shape down to 10 keV with index 2.14 and 2.8 by Sacher and Schönfelder (1984)

Appendix B

Energy spectrum of electrons in the interstellar space

B.1 Energy loss rate of relativistic electrons

The energy loss rate of the relativistic electrons by emission and ionization loss process are summarized by Hayakawa (1969) in numerical form as follows ;

$$-\frac{dE}{dt}\big|_s = 0.98 \times 10^{-3} H_\perp^2 \gamma^2 \ (ev/sec), \tag{B.1}$$

for synchrotron radiation in the magnetic field of H gauss,

$$-\frac{dE}{dt}\big|_c = 2.67 \times 10^{-14} W_{ph} \gamma^2 \ (ev/sec) \tag{B.2}$$

for inverse Compton scattering with photons of energy density W_{ph} ev/cc,

$$-\frac{dE}{dt}\big|_b = 1.37 \times 10^{-16} n_H [\ln \gamma + 0.36] E \ (ev/sec) \tag{B.3}$$

for no screening

$$-\frac{dE}{dt}\big|_b = 7.26 \times 10^{-16} n_H E \ (ev/sec) \tag{B.4}$$

for complete screening

for bremsstrahlung in the hydrogen of density n_H,

$$-\frac{dE}{dt}\big|_{ion} = 7.62 \times 10^{-9} n_H [3 \ln \gamma + 18.8] \ (ev/sec) \tag{B.5}$$

for ionization loss in the neutral hydrogen of density n_H,

$$-\frac{dE}{dt}\big|_{pl} = 7.62 \times 10^{-9} n_e [\ln \gamma - \ln n_e + 73.4] \ (ev/sec) \tag{B.6}$$

for excitation of plasma oscillation in the fully ionized medium of electron density n_e.

B.2 Qualitative interpretation of the electron spectrum

The electron energy spectrum in the interstellar space is explained qualitatively using the energy dependence of these energy loss process. We plot a sample of numerical calculation of these energy loss rate in figure B.1 assuming that the magnetic field $H_\perp = 3\mu$Gauss, the hydrogen density $n_H = 1 \ cm^{-3}$ and the photon energy density $W_{ph} = 0.4$ ev cm^{-3}. The broad solid line shows the total energy loss in the interstellar space, which is a sum of energy loss by the ionization loss, bremsstrahlung, synchrotron radiation and inverse Compton. We also plot the energy loss of electrons by escaping from the Galaxy with escape time of 3×10^{14} seconds independent to the energy. These two lines cross at two point about 100 MeV($= E_1$) and 10 GeV($= E_2$). The electrons with energy between E_1 and E_2 is governed by the escaping process.

If the injection electron spectrum is a single power-law of index p, the index is kept p between E_1 and E_2. Above E_2, the index is changed from p to $p + 1$, because the energy loss rate of synchrotron radiation and inverse Compton scattering is proportional to the electron energy. Below E_1, the spectrum is expected to be flattened by the ionization loss. This qualitative understandings of the electron spectrum in the interstellar space is shown in a schematic drawing in figure B.2
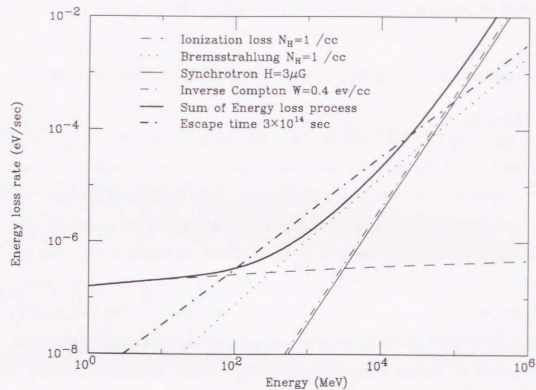
Figure B.1: A sample of calculation of energy loss rate for relativistic electrons in the interstellar matter with the magnetic field of 3μGauss, hydrogen density of $1\ cm^{-3}$, and photon energy density $0.4\ eV\ cm^{-3}$. dashed line shows the energy loss rate by ionization loss, dots line by bremsstrahlung, solid line by synchrotron radiation, dot–dashed line by inverse Compton scattering and broad solid line by the sum of above four process. broad dot-dash line means the energy loss by escaping from the Galaxy with escape time of 3×10^{14} seconds.
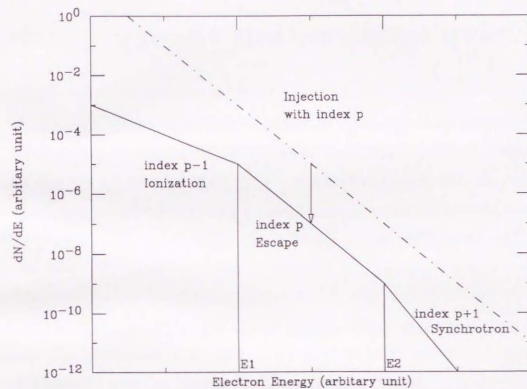
Figure B.2: A schematic view of the electron spectrum assuming injection electrons with a single power-law in the interstellar space

Appendix C

Diffusive acceleration theory

In this chapter, we briefly summarize the diffusive acceleration process applicable to the non-relativistic energy region based on Bell (1978a; 1978b) and show an expected energy spectrum of the accelerated particles.

The non-relativistic diffusive shock acceleration rate per one collision is given by equation (1) in Bell (1978b) as

$$\Delta T / T = \frac{(T + m_e c^2)}{T} \frac{4v(u_1 - u_2)}{3c^2}, \tag{C.1}$$

where, u_1, u_2, v are the velocities of upstream, downstream and particles in the shock frame.

The cycling time t_{cyc} is given by equation (3) in Bell (1978a) as

$$t_{cyc} = \frac{4}{v} \left(\frac{\kappa_1}{u_1} + \frac{\kappa_2}{u_2} \right), \tag{C.2}$$

where, κ = diffusion constant.

Then the acceleration time to obtain energy T is given by

The acceleration time to obtain energy T is approximately given by,

$$t_{acc} = t_{cyc} \times \frac{T}{\Delta T}. \tag{C.3}$$

And the acceleration rate is approximately

$$\frac{T}{t_{acc}} = \frac{\Delta T}{t_{cyc}}. \tag{C.4}$$

Then the probability of the escaping from the shock front by the diffusion is given by

$$\eta = 4 \frac{u_2}{v}. \tag{C.5}$$

And the resultant energy spectrum of accelerated particles is

$$
\begin{aligned}
N(T) &= (\mu - 1)(T_0^2 + 2E_R T_0)^{-(\mu-1)/2} (T + E_R)(T^2 + 2TE_R)^{-(\mu+1)/2} \\
&\propto (t+1)(t^2 + 2t)^{-(\mu+1)/2} \\
&\rightarrow t^{-\mu} \quad (t \gg 1)
\end{aligned} \tag{C.6}
$$

here, $N(T)$ = number spectrum of electrons,

$\mu = \frac{2u_2 + u_1}{u_1 - u_2} + O(\frac{u_1 - u_2}{c})$, power-law index at high energy ,

T = electron kinetic energy ,

T_0 = initial electron kinetic energy,

E_R = electron rest mass energy ,

and $t = T/E_R$.

Note that it does not follow a single power-law form in the non-relativistic energy band because the acceleration rate per collision is in proportion to the particle's momentum, not to the energy. A schematic drawing of the energy spectrum is shown in figure C.1 (Berezinskiĭ *et al.*, 1990). The spectrum index steepen at around the particle's rest mass energy. The mass difference between protons and electrons causes the flux difference at high energy band.
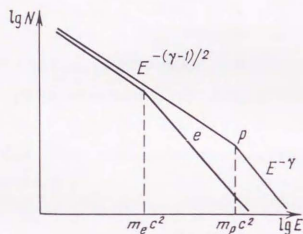
Figure C.1: The Schematic form of the energy spectra of the cosmic ray electrons and protons accelerated by a shock wave for the same injection power of non-relativistic particles (Berezinskiǐ et al., 1990).

Acknowledgment

Bibliography

Allen, C. W.: 1976, *Astrophysical Quantities*, The athlone press, 3rd edition

Bell, A. R.: 1978a, *Mon. Not. R. Astron. Soc.* **182**, 147

Bell, A. R.: 1978b, *Mon. Not. R. Astron. Soc.* **182**, 443

Berezinskiǐ, V. S. *et al.*: 1990, *Astrophysics of Cosmic Rays*, North-Holland, Translated from Russian by L. J. Reinders

Bertsch, D. L. and Kniffen, D. A.: 1983, *Astrophys. J.* **270**, 305

Bevington, P. R. and Robinson, D. K.: 1992, *Data reduction and error analysis for the physical sciecnce*, McGraw-Hill Inc., 2nd edition

Bloemen, H.: 1989, in *Annual review of astronomy and astrophysics*, Vol. 27, p. 469, Annual Reviews Inc.

Blumenthal, G. R. and Gould, R. J.: 1970, *Rev. Mod. Phys.* **42**, 237

Bouchet, L.: 1992, *Ph.D. thesis*, l'Universite Paul Sabatier

Dolan, J. F.: 1983, *List of Positions of All X-Ray Sources with Positions Known More Accurately than those Given in the 4U or 2A Catalogues*, Astrophysical Data Center NASA.GSFC, A7055 of ADC catalogues

Einstein Catalog Committee: 1990, *The Einstein Observatory Catalog of IPC X-Ray Sources*, FITS/CD-ROM version, Sumithonian Institution

Gehrels, N. and Tueller, J.: 1993, *Astrophys. J.* **407**, 597

Grabelsky, D. A. *et al.*: 1995, *Astrophys. J.* **441**, 800

Harmon, B. A. *et al.*: 1993, in N. G. M. Friedlander and D. J. Macomb (eds.), *COMPTON GAMMA-RAY OBSERVATORY*, No. 280 in AIP Conference Proceedings 280, p. 350, AIP Press

Hartman, R. C. *et al.*: 1979, *Astrophys. J.* **230**, 597

Hayakawa, S.: 1969, *Cosmic Ray Physics*, Wily Interscience

Hayashida, K.: 1989, *Ph.D. thesis*, University of Tokyo

Hayashida, K. *et al.*: 1989, *Publ. Astron. Soc. Jpn.* **41**, 373

Hertz, P. and Grindlay, J. E.: 1984, *Astrophys. J.* **278**, 137

Hirosawa, H. *et al.*: 1971, in *Proc of 9th ISTS*, Vol. 9, p. 1095

Ishida, M.: 1991, *Ph.D. thesis*, University of Tokyo

Kamae, T. *et al.*: 1992, *Proceedings of SPIE* **1734**, 2

Kniffen, D. A. and Fichtel, C. E.: 1981, *Astrophys. J.* **250**, 389

Koch, H. W. and Motz, J. W.: 1959, *Rev. Mod. Phys.* **31**, 921

Kosugi, T. *et al.*: 1992, *Publ. Astron. Soc. Jpn.* **44**, L45

Koyama, K.: 1989, *Publ. Astron. Soc. Jpn.* **41**, 665

Koyama, K., Ikeuchi, S., and Tomisaka, K.: 1986, *Publ. Astron. Soc. Jpn.* **38**, 503

Koyama, K. *et al.*: 1986, *Publ. Astron. Soc. Jpn.* **38**, 121

Koyama, K. *et al.*: 1989, *Nature* **339**, 603

Koyama, K. *et al.*: 1995, *Nature* **378**, 255

Longair, M. S.: 1994a, *High energy Astrophysics*, Vol. 2, Cambridge University Press, 2 edition

Longair, M. S.: 1994b, *High energy Astrophysics*, Vol. 1, Cambridge University Press, 2 edition

Makishima, K. *et al.*: 1989, *Publ. Astron. Soc. Jpn.* **41**, 53

Mandrou, P. *et al.*: 1980, *Astrophys. J.* **237**, 424

Masai, K.: 1984, *Astron. Astrophys. Suppl. Ser.* **98**, 367

Mayer-Hasselwander, H. A. *et al.*: 1982, *Astron. Astrophys.* **105**, 164

Miyazaki, S.: 1993, *Ph.D. thesis*, University of Tokyo

Murakami, H. *et al.*: 1992, *IEEE Trans. Nucl. Sci.* **39(5)**, 1316

Murthy, P. V. R. and Wolfendale, A. W.: 1993, *Gamma-ray astronomy*, Cambridge University Press, 2 edition

Nishimura, J. *et al.*: 1990, in R. J. Protheroe (ed.), *21st International Cosmic Ray Conference*, Vol. 3, p. 213, The University of Adelaide

Ogawara, Y. *et al.*: 1992, *Publ. Astron. Soc. Jpn.* **44**, L41

Ottmann, R. and Schmitt, J. H. M. M.: 1992, *Astron. Astrophys.* **256**, 421

Patterson: 1984, *Astrophys. J., Suppl. Ser.* **54**, 443

Paul, J. A. *et al.*: 1978, *Astron. Astrophys.* **63**, L31

Ptsukin, V. P.: 1994, in N. G. C. E. Fitchel and J. P. Norris (eds.), *The Second Compton Symposium*, No. 304 in AIP Conference Proceedings 304, p. 474, AIP Press

Purcell, W. R. *et al.*: 1995, in *3rd Compton Symposium*

Reid, M. J.: 1993, in *Annual review of astronomy and astrophysics*, Vol. 31, p. 345, Annual Reviews Inc.

Rybicki, G. B. and Lightman, A. P.: 1979, *Radiative Processes in Astrophysics*, John Willy abd Sons

Sacher, W. and Schönfelder, V.: 1984, *Astrophys. J.* **279**, 817

Shafer, R. A. *et al.*: 1992, *XSPEC An X-Ray Spectral Fitting Package,Version 2 of User's Guide*, Technical report, Goddard Space Flight Center/NASA

Shafer, R. A. *et al.*: 1994, *XSPEC 8.41 Release note*, Technical report, Goddard Space Flight Center/NASA

Skibo, J. G. and Ramaty, R.: 1993, *Astron. Astrophys. Suppl. Ser.* **97**, 145

Strong, A. W. *et al.*: 1994, *Astrophys. J., Suppl. Ser.* **92**, 425

Takahashi, T. *et al.*: 1993, *IEEE Trans. Nucl. Sci.* **40(4)**, 890

Tamura, T.: 1993, *Ph.D. thesis*, University of Tokyo

Turner, M. J. L. *et al.*: 1989, *Publ. Astron. Soc. Jpn.* **41**, 345

Verschuur, G. L. and Kellermann, K. I.: 1988, *Galactic and Extragalactic Radio Astronomy*, Springer-Verlag, 2 edition

Warwick, R. S. *et al.*: 1985, *Nature* **317**, 218

Warwick, R. S. *et al.*: 1988, *Mon. Not. R. Astron. Soc.* **232**, 551

Webber, W. R.: 1990, in R. J. Protheroe (ed.), *21st International Cosmic Ray Conference*

White, N. E.: 1994, in *New Horizon of X-ray Astronomy*, p. 9

Wood, K. S. *et al.*: 1984, *Astrophys. J., Suppl. Ser.* **56**, 507

Woosley, S. E. and Weaver, T. A.: 1986, in *Annual review of astronomy and astro-*

physics, Vol. 24, p. 205, Annual Reviews Inc.

Worrall, D. M. *et al.*: 1982, *Astrophys. J.* **255**, 111

Yamasaki, N. Y. *et al.*: 1994, in *New Horizon of X-ray Astronomy*, p. 535

Yamasaki, N. Y. *et al.*: 1995, in *3rd Compton Symposium*

Yamauchi, S.: 1991, *Ph.D. thesis*, Nagaya University

Yamauchi, S. and Koyama, K.: 1993, *Astrophys. J.* **404**, 620

Yamauchi, S. and Koyama, K.: 1995, *Publ. Astron. Soc. Jpn.* **47**, 439

Yamauchi, S. *et al.*: 1990, *Astrophys. J.* **365**, 432

Yoshimori, M. *et al.*: 1992, *Publ. Astron. Soc. Jpn.* **44**, L51